Modeling the effects of anesthesia on the electroencephalogram

I. Bojak* and D. T. J. Liley†
Centre for Intelligent Systems and Complex Processes, LSS, Swinburne University of Technology, P. O. Box 218, Hawthorn, Victoria 3122, Australia
(Received 14 October 2004; published 4 April 2005)

Changes to the electroencephalogram (EEG) observed during general anesthesia are modeled with a physiological mean field theory of electrocortical activity. To this end a parametrization of the postsynaptic impulse response is introduced which takes into account pharmacological effects of anesthetic agents on neuronal ligand-gated ionic channels. Parameter sets for this improved theory are then identified which respect known anatomical constraints and predict mean firing rates and power spectra typically encountered in human subjects. Through parallelized simulations of the eight nonlinear, two-dimensional partial differential equations on a grid representing an entire human cortex, it is demonstrated that linear approximations are sufficient for the prediction of a range of quantitative EEG variables. More than 70 000 plausible parameter sets are finally selected and subjected to a simulated induction with the stereotypical inhaled general anesthetic isoflurane. Thereby 86 parameter sets are identified that exhibit a strong "biphasic" rise in total power, a feature often observed in experiments. A sensitivity study suggests that this "biphasic" behavior is distinguishable even at low agent concentrations. Finally, our results are briefly compared with previous work by other groups and an outlook on future fits to experimental data is provided.

DOI: 10.1103/PhysRevE.71.041902 PACS number(s): 87.19.Nn, 87.19.La, 87.80.Vt, 87.18.Bb

I. INTRODUCTION

The electroencephalogram (EEG) is one of the oldest measures of brain activity and continues to be popular both in clinical practice and in research. It is a comparatively cheap, robust, and straightforward technique, but nevertheless provides data with millisecond time resolution showing clear correlations to observed mental states. Its main shortcoming is a lack of spatial resolution. The EEG is a *surface* measure; hence any depth information is necessarily derived and uncertain. Furthermore, even its two-dimensional resolution is at best in the square centimeter range [1]. However, many questions about the state of the brain do not require perfect, or even any, spatial information. The hypnotic state is a likely candidate, since the absence of pain experience and memory retention suggests that gross changes of brain function have occurred.

Despite many decades of research into the mechanisms of general anesthesia there are surprisingly few integrated theories attempting to characterize this phenomenon. This has probably been due to the fact that, until recently, there has been no real agreement on what macroscopic observables of anesthetic effect are to be modeled. However, an unquestionable indicator of the depth of anesthesia would be of paramount importance in clinical practice. In particular frail patients would benefit from precisely guided dosage. Thus it is not surprising that in the last decade or so several heuristic approaches based on electroencephalographic monitoring of depth of anesthesia have been developed [2]. The use of such monitoring has been shown to reduce the incidence of postoperative recall [3]. Hence these heuristic methods of EEG analysis represent an operational measure of the level of consciousness, albeit of unclear efficacy.

In principle then modeling the effects of anesthetic agents on EEG activity not only can help in explaining the remarkable phenomena of general anesthetic (GA) action, but also can provide an entry point for the quantitative characterization of consciousness. Methods based on the spontaneous EEG—proprietary ones like the Narcotrend value and the Bispectral Index (BIS), as well as those typical for any power spectrum analysis—have been employed with varying degrees of success. For example, Sebel *et al.* [4] found that opioid analgesics popular in actual clinical practice limit the usefulness of the BIS.

Here one encounters a problem inherent to any heuristic approach: since it is not based on a deeper understanding of underlying mechanisms, failures do not point to improvements in an obvious manner. Rather than trying to invent yet another heuristic EEG-based measure, our aim here is to provide a theoretical model for the induced changes which is based on known physiology. Our theory relates well known microscopic (cellular and subcellular) targets of GA action to their macroscopic consequences (EEG activity). In the long run this may lead to the development of a depth of anesthesia monitor based on the EEG, which can truly replace established methods like the vegetative PRST (blood pressure, heart rate, sweating, tear formation) score [5] in clinical practice.

By establishing a mesoscopic link through our model we also open up a much needed window on human physiology. Most experimental (sub)cellular data can be obtained from animal preparations only. But if such data lead to successful predictions of human EEG features, as in this paper, then one can infer similar (sub)cellular behavior of human neurons. The approach we take here differs from earlier models [6,7]

*Electronic address: ibojak@swin.edu.au; URL: http://users.on.net/ibojak
†Electronic address: dliley@swin.edu.au; URL: http://liley.bsee.swin.edu.au/~dtl/

in that we parametrize, on the basis of detailed empirical data from rat hippocampus, the effects GAs have on both cortical excitation and inhibition in the context of a theory that is based on human physiology and preserves all the essential dynamical features of human resting EEG. This level of fidelity to experimental data is necessary for conclusions about human physiology now, and for the development of medical applications in the future.

The paper begins with an overview of the theory of Liley *et al.* [8,9] for electroencephalographic rhythmogenesis. In Sec. III components of this model are then further developed, on the basis of our current understanding regarding the cellular and subcellular targets of GA agents. Section IV then comprehensively outlines a range of numerical methods and approaches needed to establish physiologically plausible model behavior and parametrization. This will enable us to meaningfully appraise our theory's response to perturbations designed to model the effects of GA agents. Section V contains the results of extensive Monte Carlo parameter space searches. The identified physiologically plausible parametrizations are shown to be capable of reproducing many features of the EEG in response to GAs. This paper then ends with a comparison of our approach with the work of others and with a discussion of the implications of our theory and results for better understanding GA action. In the appendix we tabulate two dozen of the plausible parameter sets we have found. As an outlook on future work, we also briefly compare the mean behavior of these sets with some experimental data.

II. BASIC ELECTROCORTICAL MODEL

The model of Liley *et al.* [8,9] can produce the main features of the spontaneous human EEG and mirrors at least qualitatively the effects GABA-enhancing (GABA denotes gamma-aminobutyric acid) general anesthetics have on the EEG [10]. As is appropriate for a description of EEG data, the model is spatially coarse grained. The neural activity over roughly the extent of a macrocolumn (typical diameter 0.5–3 mm [11]) is averaged to produce a "mean field" description in space. However, no averaging takes place with respect to changes in time.

A schematic representation of the model is given by Fig. 1, which depicts the model interactions taking place both within and between two different macrocolumns. Two distinct types of spatially averaged subpopulations of neurons are taken into account to subsume the actual variety of cortical cells: excitatory (E) and inhibitory (I) neurons. The interactions of these subpopulations within the macrocolumns are proportional to the number of their connections N_{lk}^{β} and their mean firing rates S_k, with $k,l=e$ (excitatory), i (inhibitory). The subscript lk means $l\rightarrow k$, i.e., type l acting on type k. Each macrocolumn can also have extracortical inputs p_{lk}, for example from the thalamus. Only the excitatory subpopulations are considered to form long-range connections Φ_{ek} to other macrocolumns, but those connections can form on both types of neurons in the target macrocolumn. In mathematical terms the model is detailed as follows:

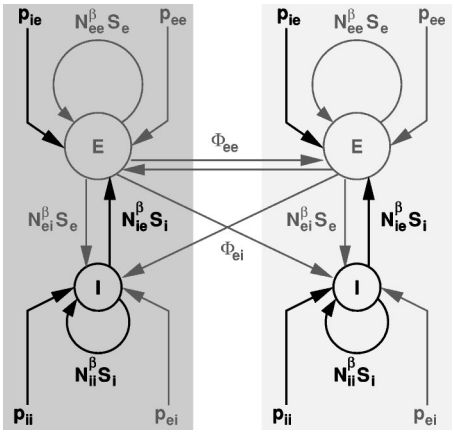

FIG. 1. A schematic illustration of the Liley *et al.* [8,9] model. Two distinct macrocolumns with their excitatory (E) and inhibitory (I) neuron populations are shown, as well as their short- and long-range cortical and extracortical connections. The labels correspond to Eqs. (1)–(6).

$$\tau_k \frac{\partial h_k(\vec{x},t+\xi)}{\partial t} = -[h_k(\vec{x},t+\xi) - h_k^r] + \sum_l \psi_{lk}(h_k) I_{lk}(\vec{x},t), \tag{1}$$

$$\psi_{lk}(h_k) = [h_{lk}^{\mathrm{eq}} - h_k(\vec{x},t+\xi)]/|h_{lk}^{\mathrm{eq}} - h_k^r|, \tag{2}$$

$$\left(\frac{\partial}{\partial t} + \gamma_{lk}\right)^2 I_{lk}(\vec{x},t) = e\Gamma_{lk}\gamma_{lk}[N_{lk}^{\beta}S_l(h_l) + \Phi_{lk}(\vec{x},t) + p_{lk}(\vec{x},t)], \tag{3}$$

$$S_k(h_k) = S_k^{\max} \Big/ \left\{1 + (1 - r_{\mathrm{abs}}S_k^{\max}) \times \exp\left[-\sqrt{2}\frac{h_k(\vec{x},t+\xi) - \overline{\mu_k}}{\hat{\sigma}_k}\right]\right\}, \tag{4}$$

$$\left[\left(\frac{\partial}{\partial t} + v\Lambda_{ek}\right)^2 - \frac{3}{2}v^2\nabla^2\right]\Phi_{ek}(\vec{x},t) = v^2\Lambda_{ek}^2 N_{ek}^{\alpha}S_e(h_e), \tag{5}$$

$$\Phi_{ik} \equiv 0. \tag{6}$$

Equation (1) describes the response of the mean soma membrane potentials h_k to synaptic inputs I_{lk}, taking into account reversal potentials via Eq. (2). Equation (3) traces these synaptic inputs to three sources: locally in the same macrocolumn of cortex, further away but within the cortex, and extracortical. Local activity is estimated with Eq. (4) using a sigmoidal dependence on the local mean membrane potential. Extracortical activity at rest is represented by physiologically shaped brown noise input via p_{lk}. Finally long-distance effects are modeled by Eq. (5), which lets activity spread omnidirectionally with speed v while decaying exponentially with a fiber scale constant Λ_{ek}. EEG voltage is expected to be linearly related to h_e, the spatially averaged excitatory soma membrane potential [8,12]. Hence h_e will be the main computational observable in the following study.

TABLE I. The physiological ranges for the 37 parameters in Eqs. (1)–(6) assumed in this paper. As shown, four parameters are set to zero and the two fiber scale parameters are set equal to each other. Furthermore, $p_{ee}=\overline{p_{ee}}$, except if there is noise input $p_{ee}=\mathcal{N}[n(\overline{p_{ee}},\delta p_{ee})]$; see Sec. IV A. This leaves 32 (or 33) independent parameters.

Parameter		Min.	Max.	Parameter		Min.	Max.
Mean resting membrane potential	h_e^r	−80 mV	−60 mV	Mean Nernst membrane potential	h_{ee}^{eq}	−20 mV	10 mV
	h_i^r	−80 mV	−60 mV		h_{ei}^{eq}	−20 mV	10 mV
Passive membrane decay time const.	τ_e	5 ms	150 ms		h_{ie}^{eq}	−90 mV	h_i^r-5 mV
	τ_i	5 ms	150 ms		h_{ii}^{eq}	−90 mV	h_i^r-5 mV
Postsynaptic potential amplitude	Γ_{ee}	0.1 mV	2.0 mV	Postsynaptic potential rate constant	γ_{ee}	100 s^{-1}	1000 s^{-1}
	Γ_{ei}	0.1 mV	2.0 mV		γ_{ei}	100 s^{-1}	1000 s^{-1}
	Γ_{ie}	0.1 mV	2.0 mV		γ_{ie}	10 s^{-1}	500 s^{-1}
	Γ_{ii}	0.1 mV	2.0 mV		γ_{ii}	10 s^{-1}	500 s^{-1}
Total number of intracortical connections	N_{ee}^{β}	2000	5000	Total number of cortico-cortical connections	N_{ee}^{α}	2000	5000
	N_{ei}^{β}	2000	5000		N_{ei}^{α}	1000	3000
	N_{ie}^{β}	100	1000	Cortico-cortical decay scale and conduction velocity	$\Lambda_{(ee=ei)}$	0.1 cm^{-1}	1 cm^{-1}
	N_{ii}^{β}	100	1000		v	100 cm/s	1000 cm/s
Maximum mean firing rate	$S_e^{\max}$	50 s^{-1}	500 s^{-1}	Rate of extracortical (noise) input	$\overline{p_{ee}}(\delta p_{ee}/\overline{p_{ee}})$	0 s^{-1} (0.1)	10^4 s^{-1} (0.25)
	$S_i^{\max}$	50 s^{-1}	500 s^{-1}		p_{ei}	0 s^{-1}	10000 s^{-1}
Firing thresholds	$\overline{\mu_e}$	−55 mV	−40 mV		p_{ie}	0 s^{-1} (fixed)	
	$\overline{\mu_i}$	−55 mV	−40 mV		p_{ii}	0 s^{-1} (fixed)	
Std. deviation of firing thresholds	$\hat{\sigma}_e$	2 mV	7 mV	Mean synaptic delay	ξ	0 ms (fixed)	
	$\hat{\sigma}_i$	2 mV	7 mV	Absolute refractory period	r_{abs}	0 ms (fixed)	

All parameters in Eqs. (1)–(6) can be related to physiological or anatomical data; see Ref. [8] for further discussion. The limits for the parameters assumed in this paper are shown in Table I. One has to specify 37 parameters for the model (plus an additional one in the case of noise input, as discussed below). We set four of these parameters to zero and assume that the scale constants for cortico-cortical excitatory fibers targeting inhibitory and excitatory subpopulations, respectively, are identical. This leaves 32 (plus one) independent parameters in the model.

A more in depth discussion of these equations can be found elsewhere [8–10]. This theory differs from other macroscopic continuum theories of electrorhythmogenesis [13–15] in that the time courses of the inhibitory and excitatory postsynaptic potentials (IPSPs and EPSPs) recorded at the soma are described by a third order differential equations. The use of lower orders to describe the IPSP are theoretically found unable to support any appreciable or widespread α band activity (for further details see Ref. [8], Appendix A).

Because this theory generates α activity through the reciprocal interaction of excitatory and inhibitory neuronal populations it does not require oscillatory thalamic input as is necessary in pacemaker accounts of cortical electrorhythmogenesis, nor does it need any explicit thalamo-cortical feedback. It is important to emphasize that this continuum *mean-firing-rate-based* theory is also "mechanistically" quite distinct from the discrete *spike-based* inhibitory interneuron network models that have been developed to investigate the genesis of synchronized γ activity and its modulation by a range of drugs [16,17].

III. EXTENSIONS FOR ANESTHESIA

The number of cellular and subcellular sites in the central nervous system at which general anesthetic agents have been shown to interact is vast [18–20]. While attempts to define a unitary mechanism of GA action have failed it has become increasingly well accepted that it is disruption in interneuronal communication that underlies their clinical actions. To date both pre- and postsynaptic targets have been identified as important in mediating the effects of GAs. In particular a large number of volatile and intravenous general anesthetic agents have been shown to interact with a range of ligand-gated ionic channels (LGICs) thereby affecting postsynaptic ionic current flow or presynaptic neurotransmitter release [21]. Studies to date have revealed $GABA_A$ and glutaminergic LGICs as the most important subcellular cortical targets for GA action at clinically relevant concentrations [22].

In general GAs have been shown to potentiate $GABA_A$-induced ionic currents and/or attenuate glutamate-mediated ionic currents [18]. From a cellular electrophysiological perspective this is seen as a prolongation of the tail of the unitary IPSP and a reduction in the peak amplitude of the EPSP [23,24]. For example, isoflurane has been shown to potentiate $GABA_A$-induced ionic currents as well as inhibiting the presynaptic release of glutamate, possibly by the activation of presynaptic kainate receptors [25]. In general GA agents from the inductive class (e.g., propofol or any of the halogenated ethers) affect $GABA_A$-mediated neurotransmission postsynaptically and glutaminergic neurotransmission presynaptically, whereas dissociative GAs (e.g., ketamine, N_2O, Xe) are currently believed to principally affect excita-

tory synaptic neurotransmission through the modulation of kainate and N-methyl-D-aspartate (NMDA) receptor function [18,19].

Macroscopically GA action can be detected using the EEG. In addition to a range of compound specific effects most GAs, at the point of loss of consciousness (LOC), are associated with low-frequency, high-amplitude activity compared with the high-frequency, low-amplitude activity while awake [26]. Following the LOC and during anesthetic maintenance the EEG spectrum is still dominated by low-frequency activity but at a magnitude generally somewhat less than during induction. This rise and fall in low-frequency power during anesthetic induction is often referred to as the "biphasic effect." Similar behavior can be observed in other frequency bands and in particular also in total power; see for example Refs. [27,28].

We will use "biphasic" as a generic label for any rise and fall of some EEG "strength" measure during a monotonic change in GA concentration. While the form of this response can show substantial agent and subject variability it is sufficiently widespread to be considered a canonical GA phenomenon. The effect of GABA-enhancing general anesthetics, like propofol or the halogenated ethers, can be approximated in the basic model by *decreasing* the appropriate decay rate constant γ_{ik} [10]. Upon lowering γ_{ik} with anesthetics, the model qualitatively predicts first an increase and then a decrease of EEG "strength" in a chosen frequency band. The reverse happens upon increasing γ_{ik} to its original value.

A. Modifying the postsynaptic response

In order to obtain more quantitative predictions of anesthetic effects, we will modify Eq. (3) here. Imagine that on its right hand side a unit presynaptic pulse $\delta(t=0)$ arrives. The postsynaptic activation I_{lk} in Eq. (3) will then show the impulse response

$$R_0(t) = e\Gamma_{lk}\gamma_{lk}te^{-\gamma_{lk}t}\Theta(t), \tag{7}$$

$$R_0(\omega) = e\Gamma_{lk}\gamma_{lk}\frac{1}{(i\omega+\gamma_{lk})^2}, \tag{8}$$

where $\Theta(t)$ is the "Heaviside theta" or unit step function and $R_0(\omega)$ is the Fourier transform of $R_0(t)$. This represents the simplest, so-called α model of "fast" excitatory [α-amino-3-hydroxy-5-methyl-4-isoxazoleproprionic acid (AMPA)/kainate] and inhibitory ($GABA_A$) neurotransmitter kinetics, respectively. Note that the maximum $R_0=\Gamma_{lk}$ occurs at $t=1/\gamma_{lk}$.

A biexponential model proportional to $(e^{-\gamma_1 t}-e^{-\gamma_2 t})$ is often used to describe experimental data, since it provides more flexibility in fitting the measured time evolution. The Fourier transform of this model is simply proportional to $(\gamma_2-\gamma_1)(i\omega+\gamma_1)^{-1}(i\omega+\gamma_2)^{-1}$. Note that the standard biexponential model vanishes for $\gamma_1=\gamma_2$. We introduce here a different kind of biexponential model:

$$R(t) = e^{\gamma_{lk}\delta_{lk}}\Gamma_{lk}\tilde{\gamma}_{lk}\frac{e^{-\gamma_{lk}t}-e^{-\tilde{\gamma}_{lk}t}}{\tilde{\gamma}_{lk}-\gamma_{lk}}\Theta(t), \tag{9}$$

$$\gamma_{lk} \equiv \frac{\varepsilon_{lk}}{e^{\varepsilon_{lk}}-1}\frac{1}{\delta_{lk}}, \quad \tilde{\gamma}_{lk} \equiv e^{\varepsilon_{lk}}\gamma_{lk}, \tag{10}$$

$$R(\omega) = e^{\gamma_{lk}\delta_{lk}}\Gamma_{lk}\tilde{\gamma}_{lk}\frac{1}{i\omega+\gamma_{lk}}\frac{1}{i\omega+\tilde{\gamma}_{lk}}. \tag{11}$$

This parametrization introduces just one additional control parameter ε_{lk} and has several compelling features. (1) It is a biexponential model with two independent first order Fourier poles at $\gamma_1=\gamma_{lk}$ and $\gamma_2=\tilde{\gamma}_{lk}$. (2) For $\varepsilon_{lk}\to 0$, $R\to R_0$, where R_0 is the α model of Eq. (7) with one second order Fourier pole at γ_{lk}. (3) The maximum is always $R(t=\delta_{lk})=\Gamma_{lk}$. This is also true for the R_0 limit, where $\delta_{lk}=1/\gamma_{lk}$. (4) $\varepsilon_{lk}\to-\varepsilon_{lk}$ leaves R invariant, thus without loss of generality $\varepsilon_{lk}\geqslant 0$. (5) $R(t)\geqslant R_0(t)$ with equality only at $t=0$, δ_{lk}. Note that $e^{\gamma_{lk}\delta_{lk}}\tilde{\gamma}_{lk}=e^{\tilde{\gamma}_{lk}\delta_{lk}}\gamma_{lk}$ and for $\varepsilon_{lk}\to-\varepsilon_{lk}$ the poles $\gamma_{lk}\leftrightarrow\tilde{\gamma}_{lk}$. Hence this factor ensures invariance.

The necessary replacement of Eq. (3) can be read off directly from the Fourier transform Eq. (11) by replacing $i\omega\to\partial/\partial t$ and multiplying out the norm for the pulses:

$$\left(\frac{\partial}{\partial t}+\gamma_{lk}\right)\left(\frac{\partial}{\partial t}+\tilde{\gamma}_{lk}\right)I_{lk}(\vec{x},t) = e^{\gamma_{lk}\delta_{lk}}\Gamma_{lk}\tilde{\gamma}_{lk}[N_{lk}^{\beta}S_l(h_l)+\Phi_{lk}(\vec{x},t)+p_{lk}(\vec{x},t)]. \tag{12}$$

Since $\tilde{\gamma}_{lk}=\gamma_{lk}=1/\delta_{lk}$ for $\varepsilon_{lk}=0$, Eq. (12) obviously reduces to Eq. (3) in this limit. The implied structural changes to a numerical computation in terms of first order ordinary differential equations (ODEs) are trivial. However, care has to be taken in the numerical evaluation of γ_{lk} for ε_{lk} close to zero. Here an appropriate Taylor expansion in ε_{lk} is used.

R specifies the biexponential fit in terms of the rise time to maximum δ_{lk} and the control parameter ε_{lk}. The limiting $\varepsilon_{lk}=0$ case yields the "sharpest" response peak around the specified δ_{lk}, i.e., the response will rise earlier but decay more slowly for larger values of ε_{lk}. We define the decay time $\zeta_{lk}>\delta_{lk}$ by $R(\zeta_{lk})\equiv\Gamma_{lk}/e$. Although an analytic form cannot be obtained, ζ_{lk} is easy to calculate numerically. We use such a numerical value in our computations. However, an excellent approximation with a relative error of less than 0.5% for all ε_{lk} is provided by

$$\zeta_{lk} = \left[0.90211 + 2\frac{\sinh\varepsilon_{lk}}{\varepsilon_{lk}} + \frac{0.30538\tanh(0.79931\varepsilon_{lk})}{\varepsilon_{lk}}\right]\delta_{lk}. \tag{13}$$

This actually represents a one-parameter fit, since the form is constrained to have the correct small and large ε_{lk} limits:

$$\zeta_{lk} \simeq \begin{cases} [3.1462+0.28135\varepsilon_{lk}^2]\delta_{lk}, & \varepsilon_{lk}\ll 1, \quad (14) \\ \left[\frac{1}{\varepsilon_{lk}}e^{\varepsilon_{lk}}\right]\delta_{lk}, & \varepsilon_{lk}\gg 1. \quad (15) \end{cases}$$

The decay time rises monotonically with ε_{lk} and beyond about $\varepsilon_{lk}\simeq 3$ grows exponentially according to Eq. (15).

Figure 2(b) demonstrates the importance of obtaining the extra control parameter ε_{lk}: If we wish to prolong the decay of the response in R_0, our only choice is to decrease γ_{lk}—thus increasing $\delta_{lk}=1/\gamma_{lk}$. This is obvious from the

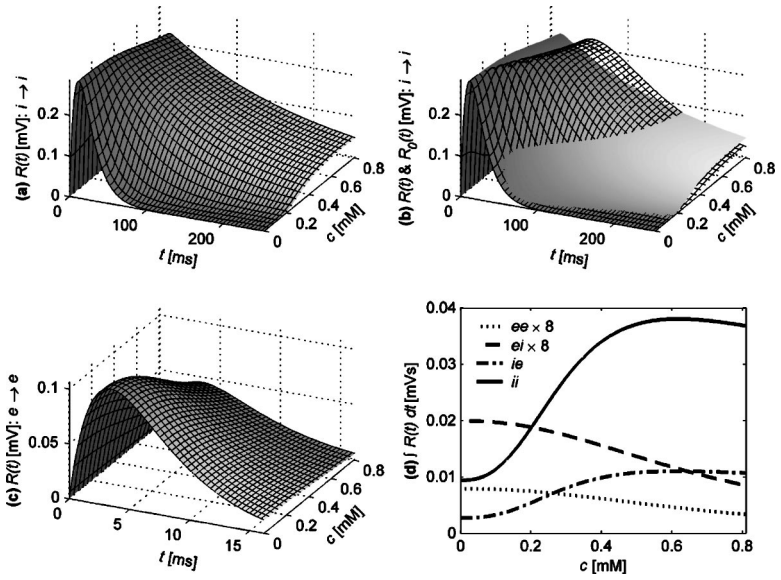

FIG. 2. (a) Response R of the inhibitory subpopulation to an inhibitory impulse depending on time and concentration of isoflurane according to Eqs. (9), (16), and (17) and Tables II and III. (b) The grid lines now represent R_0 of Eq. (7) with $\gamma_{lk}|_{R_0} = 3.1462/\zeta_{lk}(c)|_R$. R of (a) is displayed for comparison as a solid surface. (c) The response R of the excitatory subpopulation after an excitatory impulse. (d) The responses integrated over time, approximately proportional to the total charge transferred.

$\varepsilon_{lk}=0$ limit of Eq. (14): decay time $\zeta_{lk}=3.1462\delta_{lk}$. But δ_{lk} also represents the rise time $R_0(\delta_{lk})=\Gamma_{lk}$; hence for R_0 the rise time is always prolonged together with the decay time. However, for R with $\varepsilon_{lk}\neq 0$ the rise and decay times are decoupled. This is important because GAs prolong the rise time much less than the (inhibitory) decay time, if at all. Hence as Fig. 2(a) shows, we will parametrize the inhibitory $\zeta_{ik}(c)$ of R to grow with anesthetic agent concentration c, whereas $\delta_{lk}=$const. If we naively try to enforce the same $t\rightarrow\infty$ behavior for R_0 by setting the γ_{lk} of R_0 according to Eq. (10), then R_0's rise time quickly becomes unacceptable at higher concentrations.

How much better would some kind of "best fit" of R_0 to decay times fare? In Fig. 2(b) we have forced R_0 (grid lines) and R (solid surface) to have the same decay time: $\gamma_{ii}|_{R_0} = 3.1462/\zeta_{ii}(c)|_R$. But the R_0 rise time is still growing strongly with concentration and to compensate R_0 decays more quickly. Thus the entire impulse response is distorted in comparison to R. At the highest concentrations in Fig. 2(b) the R_0 rise time has still grown substantially, but in experiments the rise time is often ignored as negligible compared to the decay time. In this case the R_0 parametrization becomes simply inconsistent with the assumptions behind typical experimental fits.

B. Experimental constraints

In contrast, for R we can use experimental data concerning the postsynaptic potential amplitude and decay time under the influence of anesthetic agents. Currently, only data obtained from rat hippocampal brain slices appear to be available. Fits of the Hill equation to dose-response curves

$$\Gamma_{lk}(c) = \Gamma_{lk}\frac{K_{lk}^{N_{lk}} + M_{lk}c^{N_{lk}}}{K_{lk}^{N_{lk}} + c^{N_{lk}}}, \tag{16}$$

$$\zeta_{lk}(c) = \zeta_{lk}\frac{k_{lk}^{n_{lk}} + m_{lk}c^{n_{lk}}}{k_{lk}^{n_{lk}} + c^{n_{lk}}}, \tag{17}$$

where c is the concentration of the anesthetic agent isoflurane in blood in millimoles, were performed for IPSPs in Ref. [29]. The resulting parameters are collected in Table II. The rise time δ_{ik} was not found to be significantly affected [32]. Similarly, we use a fit of Eq. (16) to Fig. 3 in Ref. [30] for describing the concentration dependence of the EPSPs. As shown in Table II, our fit was compatible with setting $M_{ek}=0$. We assume that neither rise time δ_{ek} nor decay time ζ_{ek} is significantly affected for EPSPs, consistent with the sample time courses shown in Ref. [30] and studies of miniature excitatory postsynaptic currents [25].

Further we assume that the EPSPs are due solely to AMPA/kainate receptor mediated current flow, as the majority of NMDA receptor mediated currents in cortex are expected to be disabled as a consequence of the voltage-dependent Mg^{2+} block for the modest depolarizations associated with resting α activity [33]. Nishikawa and MacIver [31], by studying the effect of isoflurane in rat CA1, showed that non-NMDA field EPSPs were reduced by 31.7% in the presence of 0.5 mM isoflurane. Thus we adjust K_{ek} so that 68.3% of the EPSP amplitude remains at $c=0.5$ mM. Furthermore, PSP changes under anesthesia depending on the nature of the *target* neuron remain unexplored to our knowledge. Hence we will assume the same dependence in Eqs. (16) and (17) for $k=e$ and i.

Equation (16) can be used directly. The peak height Γ_{lk} of the original parametrization is inserted on the right hand side (RHS) of Eq. (16) to obtain the $\Gamma_{lk}(c)$ of the corresponding

TABLE II. Isoflurane parameters for Eqs. (16) and (17) according to Ref. [29] for $l=i$ and Refs. [30,31] for $l=e$. The same values are assumed for $k=e,i$ and $\zeta_{ek}=$const.

Isoflurane parameter	$l=e$	$l=i$
K_{lk} (mM)	0.707	0.79±0.24
M_{lk}	0.0	0.56±0.13
N_{lk}	2.22	2.6±0.8
k_{lk} (mM)		0.32±0.05
m_{lk}		4.7±0.5
n_{lk}		2.7±1.2

anesthesia parametrization at concentration c. However, Eq. (17) is used indirectly. The decay time ζ_{lk} of the original ($\varepsilon_{lk}=0$) parametrization is inserted on the RHS of Eq. (17) to obtain the corresponding $\zeta_{lk}(c)$ at concentration c. Then we calculate from $\zeta_{lk}(c)$ the $\varepsilon_{lk}(c)$ needed to prolong the original decay time accordingly. To put it differently, one equates the RHSs of Eqs. (17) and (13), inserts the δ_{lk} and $\zeta_{lk}=3.1463\delta_{lk}$ of the original parametrization, and then solves for ε_{lk} at a given concentration c. This $\varepsilon_{lk}(c)$ is then used for the anesthesia parametrization. However, in practice we calculate $\varepsilon_{lk}(c)$ numerically without the approximation in Eq. (13).

What is a reasonable range for c, the anesthetic agent concentration in blood? We follow Ref. [34] and assume that 1.3 vol % inhaled isoflurane leads to an aqueous concentration $c=0.27$ mM at body temperature $T=37\,^{\circ}$C. A measure commonly employed in anesthetic practice is the minimum alveolar concentration (MAC) of anesthetic agent at 1 atm pressure. At 1 MAC 50% of recipients still move in response to a noxious stimulus, typically an incision. In this paper we use 1 MAC=1.17 vol % for isoflurane. This is appropriate for a human 40 years of age [35] and corresponds to $c=0.243$ mM aqueous concentration. During surgery a patient would be maintained typically at 0.9 to 2.2 MAC isoflurane in an oxygen–70% nitrous oxide mixture, or at 1.3–3 MAC without the nitrous oxide. If the anesthetic induction is performed with isoflurane, it generally commences at low levels around 0.4 MAC and is then increased to maintenance level.

In the following we will typically investigate concentrations c up to the equivalent of 3.33 MAC, that is, $c=0-0.81$ mM. Figure 2(a) shows the time course of an IPSP of the inhibitory subpopulation for concentrations up to 0.81 mM (3.33 MAC) using the isoflurane experimental data. Similarly, Fig. 2(c) displays the EPSP of the excitatory subpopulation. Figure 2(d) shows the area (in time) under the different PSPs depending on concentration. If the membrane potential h_k stayed constant, this area would be proportional to the total charge transferred. For the PSP from a single impulse this is a good approximation. We see the lowering of the peak height in both IPSP and EPSP. However, decay times are only prolonged for the IPSP, leading to drastically modified relative timing at high concentrations: $\zeta_{ii}(0\ \mathrm{m}M)=3.54\zeta_{ee}(0\ \mathrm{m}M)$, but at 2 MAC $\zeta_{ii}(0.486\ \mathrm{m}M)=13.4\zeta_{ee}(0.486\ \mathrm{m}M)$.

As is evident from the Fig. 2(d), EPSP charge transfer diminishes steadily. However, IPSP charge transfer rises quickly to a plateau before slowly falling. This is due to the competing effects of prolonging decay times and decreasing peak height. We see that the timing and charge transfer of the PSPs enter a quasistatic stage for $c\gtrsim 0.4$ mM. Intriguingly, this corresponds closely to the concentrations used for maintenance in clinical practice. For $c\to\infty$ $\Gamma_{ek}(\infty)=0$, $\zeta_{ek}(\infty)=\zeta_{ek}(0)$ but $\Gamma_{ik}(\infty)=0.56\Gamma_{ik}(0)$, $\zeta_{ik}(\infty)=4.7\zeta_{ik}(0)$. This obviously yields zero for the EPSPs, and the area of the IPSPs of Fig. 2(d) becomes 0.0083 mV s (*ie*) and 0.028 mV s (*ii*), respectively. Thus at some high concentration of anesthetic agent we expect cortex to stop being excitable tissue and enter an unresponsive state.

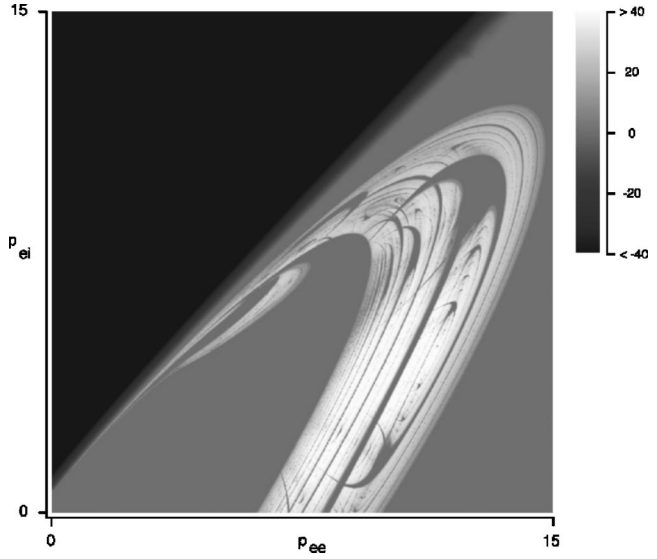

FIG. 3. Dependence of the largest Lyapunov exponent of Eqs. (1)–(6) in the homogeneous case [36]. The units of the axes are 1 ms^{-1}. This illustrates the "fat fractal" dependence of model dynamics on parameters p_{ee} and p_{ei}.

IV. ENFORCING PHYSIOLOGICAL FIDELITY

As discussed in Sec. II all 37 parameters contributing to Eqs. (1)–(6) and (12) can be related to physiological or anatomical data. It is an advantage that such experimental constraints exist external to the conception and formulation of the model. However, the parameter ranges so derived (see Table I), are currently far too large to guarantee physiological behavior for all solutions. Future advances may reduce the ranges, but it is highly unlikely that this problem will then be eliminated completely.

The external constraints on one parameter are assumed independent of the constraints on another. This is implied in just stating upper and lower bounds for all parameters, and hence in specifying a hypercube in parameter space. But in reality we expect these parameters to be interrelated in unknown ways; hence parameters representing real human cortices would necessarily map out a much more complex shape in parameter space. Furthermore, the simplifications and assumptions necessary in creating our, or indeed any, model mean that the mapping of experimental data to model parameters is approximate. Thus even perfect experimental data would not necessarily specify the region of physiological relevant parametrizations with precision.

Experience with our model shows that it has very rich dynamics which are generally unpredictable in advance; for illustration see Fig. 3. Hence it is necessary to find ways of rapidly trialing parametrizations and this section will describe in detail how this can be achieved.

A. Basic considerations

We usually start from initial conditions that are homogeneous over the entire simulated cortex. In cases where a linear approximation is viable, we use a stable "singular point" of the parameter set for the initial values of the state vari-

ables. Singular points are obtained by solving Eqs. (1)–(6) and (12) with all derivatives, temporal and spatial, set to zero. This is equivalent to solving the following two normalized equations:

$$x_e + \frac{y_{ee} - x_e}{|y_{ee}|}\left(\frac{S_{ee}}{1 + r_e e^{-(x_e - u_e)/v_e}} + P_{ee}\right) + \frac{y_{ie} - x_e}{|y_{ie}|}\left(\frac{S_{ie}}{1 + r_i e^{-(x_i - u_i)/v_i}} + P_{ie}\right) = 0, \tag{18}$$

$$x_i + \frac{y_{ei} - x_i}{|y_{ei}|}\left(\frac{S_{ei}}{1 + r_e e^{-(x_e - u_e)/v_e}} + P_{ei}\right) + \frac{y_{ii} - x_i}{|y_{ii}|}\left(\frac{S_{ii}}{1 + r_i e^{-(x_i - u_i)/v_i}} + P_{ii}\right) = 0, \tag{19}$$

with $[x_k, y_{lk}, u_k] \equiv [h_k, h_{lk}^{\mathrm{eq}}, \overline{\mu_k}]/h_k^r - 1$, $r_k \equiv 1 - r_{\mathrm{abs}} S_k^{\max}$, $v_k \equiv \hat{\sigma}_k/(\sqrt{2}h_k^r)$, $[S_{l=e,k}, S_{l=i,k}, P_{lk}] \equiv (e^{\gamma_{lk}\delta_{lk}}\Gamma_{lk}/\gamma_{lk}h_k^r)[(N_{ek}^{\alpha} + N_{ek}^{\beta})S_e^{\max}, N_{ik}^{\beta} S_i^{\max}, p_{lk}]$. In practice, Eq. (18) is solved algebraically for x_i and inserted in Eq. (19). Then zero crossings in x_e are searched for numerically.

We only accept mean firing rates between 0.1 and 20 s^{-1} as physiological. This translates directly into a restricted search range for x_e, e.g., $x_e^{\min} = u_e - v_e \ln\{[S_e^{\max}/(20\ \mathrm{s}^{-1}) - 1]/r_e\}$ rather than $x_e^{\min} = y_{ee}$. Detected zero crossings that result in inhibitory firing rates outside the physiological range are discarded. In case there are several stable singular points, we chose the one with the smallest x_e, i.e., the one closest to "rest." From the x_e and x_i we can derive the initial conditions for h_k, I_{lk}, and Φ_{ek}. If a parameter set does not have a singular point satisfying all criteria, or if we cannot assume the validity of linear approximations, we simply use "resting" initial conditions: $h_k = h_k^r$ and $I_{lk} = \Phi_{ek} = 0$. All state variable derivatives are always set to zero initially.

As is obvious from the equations, these initial conditions on their own would result in complete stasis. However, we then vary the excitatory extracortical input p_{ee} according to a random Gaussian normal distribution $n(\overline{p_{ee}}, \delta p_{ee})$. That we use such noise as "input" to the brain reflects three issues. First, we wish to simulate the simple case of a resting brain, which is not engaged in either extracting structured information from sensory data or manipulating it. Second, even if structure remained in the extracortical input, at least some of it would be lost in averaging over macrocolumns. Third, we simply do not know what sort of structured input the brain is in reality receiving. Hence using noise avoids introducing any assumption at all beyond the obvious one that the inputs will change with space and time. As simple Gaussian white noise would vary in an unphysiological manner, it is further shaped. Symbolically we can write $p_{ee}(\vec{x}, t) = \mathcal{N}[n(\overline{p_{ee}}, \delta p_{ee}), \vec{x}, t]$, with a spatiotemporal filter $\mathcal{N}$.

The finite impulse response filter in time is realized by a Remez filter of length 21, with a passband for frequencies f from 0 to 50 Hz and a stopband above 100 Hz. The 3 dB point is at $f_c = 75$ Hz. Thus time variations with unreasonably high frequencies are suppressed. The spatial filtering is performed in the Fourier domain, using a passband for $k/(2\pi)$ from 0 to 1.75 cm^{-1} and a stopband above 2.25 cm^{-1}. Between those two a cosine half period is inserted such that the 3 dB point is at $k_c/(2\pi) = 2\ \mathrm{cm}^{-1}$. Thus regions of roughly 0.5 cm diameter are driven by the same noise signal, but are uncorrelated to more distant regions. This corresponds to the assumption that one afferent fiber provides the dominant extracortical input to 1–2 macrocolumns. Finally, any negative values still remaining are set to zero.

As the creation, filtering, and distributing of noise is computationally demanding, we currently only fill p_{ee} with brown noise. p_{ei} is set to a constant, whereas p_{ie} and p_{ii} are assumed to be zero. One can speculate that connections from thalamus to cortex are predominantly excitatory. But the effects on the model of changes to the p_{lk} are correlated anyway. For example, inhibitory input to excitatory neurons p_{ie} can be taken into account partially by a reduction of excitatory input to the same excitatory neurons p_{ee}. Thus our choice of noise driving represents a reasonable first approximation.

If we can start from "singular point" initial conditions, this avoids a transient period which can otherwise last several seconds before the simulated cortex settles down into the behavior "typical" for the chosen parameter set. The possible dynamics of this system are rich indeed. It is for example not difficult to find chaotic solutions [36,37]. As mentioned, the current constraints on the parameters of Eqs. (1)–(6) and (12) are not tight enough to allow physiologically sensible solutions only. We can easily find solutions with spectral content or firing rates which bear no resemblance to those of human brains at all, or at best remind us of unusual brain states like an epileptic seizure.

B. Swarm search of homogeneous equations

Thus we are searching for parameter sets within the physiological ranges shown in Table I, which lead to reasonable excitatory and inhibitory firing rates and to a Fourier power spectrum with the major features of a resting EEG: strong activity at δ and α frequencies. We use Eq. (3) rather than Eq. (12) in the search, since we are looking for a proper baseline EEG prior to anesthesia. The gross features of the solution can usually be obtained by solving a spatially homogeneous system, i.e., experience suggests that frequency power spectra and firing rates are often qualitatively similar to those of an inhomogeneous case with the same parameters. Thus we set $h_k(\vec{x}, t) \equiv h_k(t)$ and similarly for all the other quantities. Consequently, the same p_{ee} noise is assumed everywhere and the spatial part of noise shaping is omitted. This corresponds to a "$k = 0$" spatial Fourier mode and means the Laplacian in Eq. (5) is eliminated, yielding a set of one-dimensional ordinary differential equations. We solve the ODEs just like the full set of partial differential equations (PDEs), which is discussed in detail below.

In the homogeneous case, the separate dependence on conduction velocity and fiber scale is reduced to a dependence on their product $v\Lambda_{ek}$. That still leaves 32 independent parameters in Table I to be varied within the shown ranges in order to find appropriate solutions. Parameters are held constant during the entire simulation time. Unfortunately, prior investigations had already shown that the dependence of the

solutions on these parameters is entirely nontrivial. A striking example is provided by Fig. 3. It shows the largest Lyapunov exponent of the system depending on p_{ee} and p_{ei}, while the other parameters remain fixed [36]. A 32-dimensional parameter space of such complexity is hopeless to search with even sophisticated conventional minimization algorithms like MINUIT [38], in particular since it takes a relatively long time to evaluate any specific parameter choice.

Instead we employ a different type of algorithm called particle swarm optimization (PSO) [39], which is inspired by the search strategies of swarms in nature. An "off-the-shelf" version [40] of the algorithm can be stated concisely. Assume p particles distributed in a d-dimensional parameter space. Their current positions are given by d-dimensional $\vec{x}_i$ with $i=1,\ldots,p$. Each particle memorizes its best position $\vec{b}_i$ visited so far. Furthermore, all particles know the global best position $\vec{g}$ ever visited by any particle. At every time step "velocities" $\vec{v}_i$ and positions are updated as follows:

$$\vec{v}_i(t+1) = \vec{v}_i(t) + C\{\vec{v}_i(t) + \phi_{\mathrm{cog}}[\vec{b}_i(t) - \vec{x}_i(t)] + \phi_{\mathrm{soc}}[\vec{g}(t) - \vec{x}_i(t)]\}, \tag{20}$$

$$\vec{x}_i(t+1) = \vec{x}_i(t) + \vec{v}_i(t+1), \tag{21}$$

where $\phi_{\mathrm{cog}}=\mathrm{rand}(0,\phi_{\mathrm{cog}}^{\max})$ and $\phi_{\mathrm{soc}}=\mathrm{rand}(0,\phi_{\mathrm{soc}}^{\max})$. These functions represent the weights given to individual cognition versus social interaction. Using $\phi \equiv \phi_{\mathrm{cog}}^{\max}+\phi_{\mathrm{soc}}^{\max} > 4$, the constriction factor can be written as $C=2/|2-\phi-\sqrt{(\phi-4)\phi}|$. It slows down the swarm toward convergence. We set $\phi_{\mathrm{cog}}^{\max}=2.8$ and $\phi_{\mathrm{soc}}^{\max}=1.3$, updating is asynchronous, particles stop cold at parameter boundaries, and we use about 30–60 particles [40]. We have invented several improvements over this basic implementation, which will be presented elsewhere [41].

The cost function of our PSO is calculated as follows: 25 time series of 10 s length are collected for the current parameter set. We start from "resting" initial conditions and discard all but the last 4.096 s to eliminate any transients. Firing rates are costed according to distance from the target range $0.1-20\ \mathrm{s}^{-1}$. Next the average, normalized Fourier power spectrum is fitted with a function that combines a Lorentzian resonance at $f=f_R$ of quality Q with a (bounded) power law decay f^{-B}, i.e.,

$$S(f) = \frac{A}{1+4Q^2(1-f/f_R)^2} + \frac{DC^B}{f^B+C^B}, \tag{22}$$

where D is eliminated by normalization. We force all fit parameters to stay in a reasonable range, e.g., restricting f_R to [8.5 Hz, 12.5 Hz] and B to [0.8,2.2] represents the α resonance and δ shape, respectively. Next the parameter set is costed according to the deviation of the generated spectrum from its best reasonable fit. This sort of "friendly" scoring, which first moves the functional *target* as close as possible to the result, facilitates the approach to reasonable spectra greatly. Using this method we were able to generate 33 promising parameter sets.

C. Full grid simulations

To check that these parameter sets also work for the PDEs, a full simulation of the PDEs of Eqs. (1)–(6) and (12) is performed. Equations (1)–(4) and (12) are first transformed to a set of first order ODEs and then solved by forward Euler iterations. However, Eq. (5) is iterated directly in second order, using three time points $\partial^2\Phi_{ek}(t)/\partial t^2 \simeq [\Phi_{ek}(t+\Delta t)-2\Phi_{ek}(t)+\Phi_{ek}(t-\Delta t)]/\Delta t^2$. The two-dimensional Laplacian is similarly computed on five space points with spacing $\Delta s=1$ mm. Thus the fields represent the spatial mean over 1 mm^2, or about 10^4-10^5 neurons. We simulate a square cortical sheet of realistic human size, 51.2×51.2 cm^2, and thus need 512×512 grid points. As any part of the cortex can connect to any other part, the boundaries of this square grid are connected to form a toroid. Equation (5) implies an isotropic, roughly exponential decay of connectivity. Until we introduce a more sophisticated representation of brain connectivity, toroidal boundary conditions guarantee that no point on the cortical grid connects differently from the others.

We find that for conduction velocities up to $v=10$ m/s, $\Delta t=50\ \mu$s is sufficiently short to achieve stable and convergent solutions. However, a 20 s simulation recording all grid point values for the entire state at all time steps would require about three terabytes of hard disk space. Instead we just record one state variable, usually h_e, which is directly proportional to the predicted EEG amplitude. Furthermore, we record time frames only every 2 ms. Finally we sum square patches of 16×16 grid points (1.6×1.6 cm^2) and output only the resulting 32×32 sums of each frame. Of course, real EEG electrodes also sum the signals of several square centimeters of underlying cortex and sample at around 500 Hz. The summation is a linear operation; hence it does not influence the predicted power spectra except for the statistical errors. The reduction in time resolution limits the Nyquist frequency to 250 Hz, but the main features of the human EEG reside at much lower frequencies anyway. Using these data reduction measures, the same simulation can be recorded with only 39 megabytes of hard disk space, which is manageable.

We have written the simulation code in MPI FORTRAN [42] to parallelize the calculation. The square cortical sheet is split in rectangular areas, typically 32 areas of 128×64 grid points each. Each area is assigned to one computing node for calculation. The only communication required between the nodes is concerning the one-point-deep edges of their areas. The reason is that the only spatial coupling results from the Laplacian, which requires only knowledge of the four nearest neighbors in two dimensions. For example, of the area to its left a node needs to know only the rightmost edge in order to compute the Laplacian at its own leftmost edge.

All nodes obtain their initialization data from, and send their frame output to, a central node, which performs the hard disk operations. Finally, one extra node acts as noise server. It performs the spatial noise shaping for the entire cortex, splits the noise according to the area setup, and sends the pieces to the appropriate area nodes. The received noise piece is then shaped in time at each area node. We have found that going beyond 64 areas will not improve perfor-

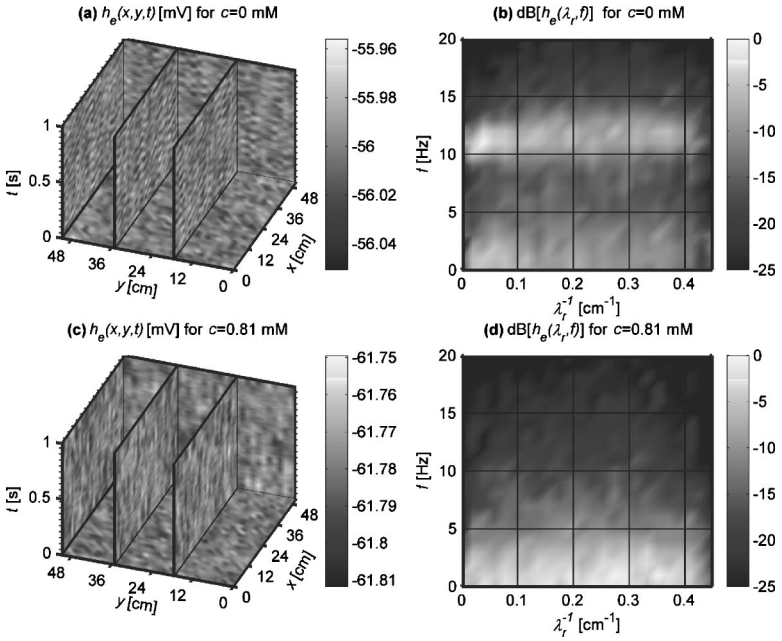

FIG. 4. (a) One second of h_e data from a full grid simulation using the parameters of Table III. The base shows the entire grid (32×32 values, interpolated) at one point in time; the vertical slices show the development with time (500 samples). (b) Radial spectrum of these data (24×21 values, interpolated) in decibels. (c) and (d) show the same as (a) and (b), respectively, but for a fully anesthetized state ($c=0.81$ mM isoflurane).

mance anymore, as communication lags limit throughput. We generally use 16 or 32 nodes, since the Swinburne and VPAC clusters are not dedicated exclusively to our computations.

It is advantageous to compute the spatial noise shaping in the Fourier domain. Assume f_{lk} with $l=0,\ldots,N_x-1$ and $k=0,\ldots,N_y-1$ to denote the real, independent, identically distributed, zero-mean Gaussian random variables on an $N_x\times N_y$ grid with N_x and N_y even. Their discrete Fourier transform (DFT) is given by

$$F_{mn}=R_{mn}+iI_{mn}=\sum_{l=0}^{N_x-1}\sum_{k=0}^{N_y-1}f_{lk}e^{-2\pi i(ml/N_x+nk/N_y)}. \quad (23)$$

The expectation value for correlations of the grid random variables $E[f_{lk}f_{l'k'}]=\sigma_f^2\delta_{l,l'}\delta_{k,k'}$. It follows that

$$E[R_{mn}R_{op}]=\frac{1}{2}N_xN_y\sigma_f^2[\delta_{m,o}^{N_x}\delta_{n,p}^{N_y}+\delta_{m,-o}^{N_y}\delta_{n,-p}^{N_y}],$$

$$E[I_{mn}I_{op}]=\frac{1}{2}N_xN_y\sigma_f^2[\delta_{m,o}^{N_x}\delta_{n,p}^{N_y}-\delta_{m,-o}^{N_y}\delta_{n,-p}^{N_y}],$$

$$E[R_{mn}I_{op}]=E[I_{mn}R_{op}]=0, \quad (24)$$

with a "modulo" Kronecker delta $\delta_{a,b}^N$ equal to 1 for $(a-b)$ mod $N=0$ and zero otherwise. Since the F_{mn} are periodic, they can be restricted to an $N_x\times N_y$ grid. Furthermore the f_{lk} are real; hence $F_{N_x-m,N_y-n}=F_{mn}^*$.

Thus the independent F_{mn} consist of N_xN_y real, independent, zero-mean Gaussian random variables filling four real $F_{mn}=R_{mn}$ at the "corners" $(m,n)=\{(0,0);(0,N_y/2);(N_x/2,0);(N_x/2,N_y/2)\}$ and $N_xN_y/2-2$ complex F_{mn}. Their variances are

$$\mathrm{var}[R_{mn}]=E[R_{mn}^2]=\frac{1}{2}N_xN_y\sigma_f^2\begin{cases}2, & \text{corners},\\ 1, & \text{others},\end{cases}$$

$$\mathrm{var}[I_{mn}]=E[I_{mn}^2]=\frac{1}{2}N_xN_y\sigma_f^2\begin{cases}0, & \text{corners},\\ 1, & \text{others}.\end{cases} \quad (25)$$

Hence we can construct the f_{lk} by filling the F_{mn} with appropriately distributed noise and then performing the inverse DFT.

The spatial filter can be implemented as a simple *multiplication* in the Fourier domain prior to the inverse DFT. Total power is conserved by normalizing by the sum of squares of the filter coefficients. In our case then the noise server has to generate 512×512 Gaussian random variables with variances as in Eq. (25), multiply each with the appropriate filter coefficient, perform the inverse DFT, cut the result up into typically 32 areas and send them to appropriate area nodes. As this is time consuming, we only generate and distribute new noise at every frame (2 ms), not at every time step (5×10^{-5} s). This is unproblematic, since the noise is low-pass-filtered in time anyway, with frequencies higher than 100 Hz eliminated. It is even helpful, since the Remez time filter can be realized with much fewer coefficients if the stopband starts at 40% instead of 1% of Nyquist frequency.

A typical example of the grid output is shown in Fig. 4(a). The value of the state variable h_e is shown by the different gray scales as indicated by the bar. On the horizontal base we show the activity of the complete 51.2×51.2 cm^2 cortical sheet at one point in time. We can see a spatial structure of synchronized activity consisting in centers and filaments extending over several centimeters. Vertical time slices show how the activity along five fixed lines on the cortical sheet changes during one second. The α rhythm is easily discernible in the "striped" structure dominating the time slices. It is more difficult to spot directly the low-frequency δ and θ activity, partly because only 1 s of data is shown.

In order to see the spatiotemporal content more clearly, we perform a three-dimensional Fourier transform of the data. Note that the toroidal grid is periodic in space as required for the Fourier transform. We subtract the overall

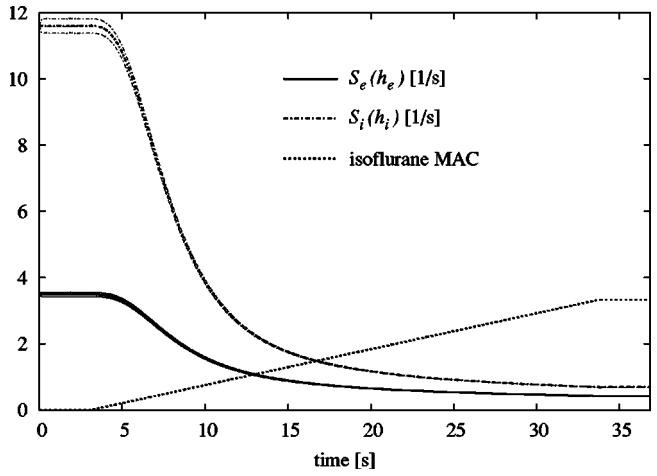

FIG. 5. Excitatory $S_e(h_e)$ and inhibitory $S_i(h_i)$ firing rates during a full grid simulation with the parameters of Table III and changing isoflurane concentration, with $c(1\ \mathrm{MAC})=0.243\ \mathrm{m}M$. The bands indicate the mean and standard deviation over all grid points.

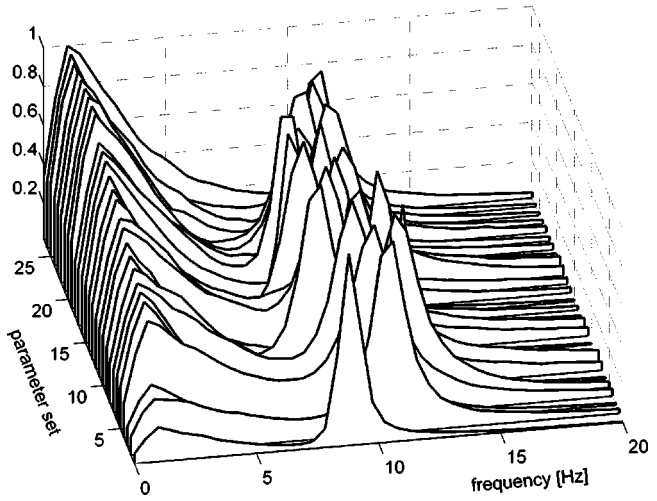

FIG. 6. Normalized power spectra obtained through full grid simulations with 27 PSO parameter sets.

mean and then multiply the time series of each grid point individually with a Hanning window to obtain periodicity in time. We can then compute a three-dimensional power spectrum $|h_e(k_x/2\pi,k_y/2\pi,f)|^2$. But a two-dimensional plot is more accessible, so for every (discrete) point (m,n) in Fourier space we compute an integer "radius" $r=\mathrm{round}[(m^2+n^2)^{1/2}]$ and then keep only the maximum power spectrum value encountered for that radius. Thereby we obtain a radial power spectrum $|h_e(\lambda_r^{-1},f)|^2$, with $\lambda_r^{-1}=r/(51.2\ \mathrm{cm})$. In Fig. 4(b) we show the result in decibels according to the gray-scale bar (all values $\leqslant -25$ are colored black).

The radial power spectrum can be misleading close to zero and maximum λ_r^{-1}, where the number of sampled points is small. Also the detrending and windowing cancels power around zero frequency. Thus one should disregard the edges of the plot. We can clearly see the strong α and δ frequency components, separated by a "valley" of lower θ activity. α activity is prominent at all wavelengths with a maximum around $\lambda_r \simeq 26$ cm. δ activity also occurs at all wavelengths with a maximum at large wavelengths. However, the dependence of the radial power spectra on wavelength varies considerably from set to set. This dependence could become a selection criterion in the future. In Figs. 4(c) and 4(d) we show for comparison a fully anesthetized state (3.33 MAC isoflurane) based on the same parameter set. The former α activity has shifted into the δ frequency range and merged with the former δ activity there. Furthermore, the merged activity is now distributed quite evenly over all wavelengths.

In Fig. 5 we show the actual time course of isoflurane concentration used in the grid simulation. The grid data in Fig. 4 correspond to the last second of the "flat" initial 0 MAC ($c=0\ \mathrm{m}M$) and final 3.33 MAC ($c=0.81\ \mathrm{m}M$) phases, respectively. The concentration is raised with each simulation time (not frame) step by the appropriate amount to obtain an overall "linear" rise. As we can see, both excitatory and inhibitory firing rates drop with increased concentrations of anesthetic agent. This is universally the case for the parameter sets investigated here.

If the concentration is raised at every frame instead of time step by a proportionally larger amount, one observes minute transient "ringing" in the firing rates. Stepping directly from zero to high concentration results in large oscillations. However, after the oscillations die down the same final (average) steady state results. If the total rise time of the concentration shown in Fig. 5 is reduced much further, large amplitude oscillations occur even with changes at every time step. While it is of interest to explore this sensitivity to rapid concentration changes, we will defer this here. Clearly, 0–3.33 MAC equivalent isoflurane blood concentration in approximately 30 s is already much more rapid than the real inductions we wish to simulate. However, *longer* concentration rise times yield the same results relative to concentration and hence are wasteful computationally.

We can now investigate the 33 parameter sets found by the swarm algorithm. It turns out that 27 of these sets yield acceptable power spectra when simulated on a full grid. For every parameter set the full 512×512 grid is run for 10 s and every 2 ms 32×32 "electrode" values are sampled. Only the last 4.096 s of these time series are kept, and individually Fourier transformed with 2.048 s, 50% overlapping, detrended Hanning windows. The normalized average yields the curves shown in Fig. 6.

The spectra vary considerably, sampling the full range of spectra encountered in humans. Furthermore, an analysis of the parameter sets shows that in *all* 27 cases a linear approximation is possible; see the next subsection. These results are by no means expected *a priori*, since the equations themselves are nonlinear in nature and the search method did *not* have any bias toward linear solutions. Thus we can reasonably investigate our equations in linear approximation without unduly constraining the type of solutions found. Of course, linear approximations offer tremendous advantages with regard to analytic and numerical computations.

D. Linear approximation and eigenspectra

We start by defining a 14-dimensional state variable vector

$$\vec{S} \equiv (h_e, h_i, I_{ee}, \tilde{I}_{ee}, I_{ei}, \tilde{I}_{ei}, I_{ie}, \tilde{I}_{ie}, I_{ii}, \tilde{I}_{ii}, \Phi_{ee}, \tilde{\Phi}_{ee}, \Phi_{ei}, \tilde{\Phi}_{ei})^T. \tag{26}$$

Here we set $\tilde{I}_{ee} = \partial I_{ee}/\partial t$ and so forth for all variables marked with a tilde. The dependence on space and time $\vec{S}(\vec{x},t)$ is implied here and in the following. These "tilde" equations together with Eqs. (1)–(6) and (12) yield

$$\frac{\partial \vec{S}}{\partial t} = \vec{F}(\vec{S}) + \vec{P}. \tag{27}$$

For example the third component of the RHS function vector $\vec{F}(\vec{S})$ is given by $F_3(\vec{S}) = \tilde{I}_{ee}$ and its fourth component $F_4(\vec{S}) = -(\gamma_{ee} + \tilde{\gamma}_{ee})\tilde{I}_{ee} - \gamma_{ee}\tilde{\gamma}_{ee} I_{ee} + e^{\gamma_{ee}\delta_{ee}}\Gamma_{ee}\tilde{\gamma}_{ee}[N_{ee}^{\beta} S_e(h_e) + \Phi_{ee} + \overline{p_{ee}}]$. Here $\overline{p_{ee}}$ means the average of the filtered noise $p_{ee}(\vec{x},t) = \mathcal{N}[n(\overline{p_{ee}}, \delta p_{ee}), \vec{x}, t]$. The vector $\vec{P}$ is zero except for components which reflect spatiotemporal *change* in the extracortical input. Thus in this paper only the fourth component is nonzero and contains the noise variation $P_4(\vec{x},t) = e^{\gamma_{ee}\delta_{ee}}\Gamma_{ee}\tilde{\gamma}_{ee}[p_{ee}(\vec{x},t) - \overline{p_{ee}}]$. Components 6, 8, and 10 of $\vec{P}$ will be zero here, because we assume other extracortical input to be static or zero.

As mentioned above, Eqs. (18) and (19) can be used to compute the singular points of our equations for a specific parameter set. Thus one obtains those singular point values $h_k = h_k^*$, $I_{lk} = I_{lk}^*$, and $\Phi_{ek} = \Phi_{ek}^*$ for which all time derivatives in Eqs. (1)–(6) and (12) vanish. With these values we can write a singular point state vector $\vec{S}^*$ for which $\vec{F}(\vec{S}^*) = 0$. Now we define $\vec{s}(\vec{x},t) \equiv \vec{S}(\vec{x},t) - \vec{S}^*$ and expand $\vec{F}$ around $\vec{S}^*$ to first order in $\vec{s}$. This yields a vector equation entirely linear in $\vec{s}(\vec{x},t)$. A spatial Fourier transform then becomes straightforward and leads to the final result by allowing us to replace the Laplacian :

$$\frac{\partial \vec{s}(\vec{k},t)}{\partial t} \simeq \mathcal{J}\,\vec{s}(\vec{k},t) + \vec{P}(\vec{k},t), \tag{28}$$

$$\mathcal{J} \equiv \left.\frac{\partial \vec{F}(\vec{S})}{\partial \vec{S}}\right|_{\substack{\vec{\nabla}^2 \to -\vec{k}^2 \\ \vec{S}=\vec{S}^*}}. \tag{29}$$

Thus $\mathcal{J}$ is simply the 14×14 Jacobian matrix evaluated at $\vec{S}^*$ upon formally replacing $\vec{\nabla}^2 \to -\vec{k}^2$. Its components are easily calculated, for example $\mathcal{J}_{14,13} = -v^2(\Lambda_{ei}^2 + \frac{3}{2}\vec{k}^2)$. Obviously in the case of spatially homogeneous $\vec{s}(\vec{x},t) = \vec{s}(t)$ Eqs. (28) and (29) hold true with $\vec{k}^2 \to 0$ and could be derived without the spatial Fourier transform.

In order for the approximation in Eq. (28) to be relevant practically, it should be stable: small disturbances $\vec{s}$ should return to zero with time. In that case the time development of Eq. (28) will approximate that of Eq. (27) provided the initial state is close to $\vec{S}^*$ and disturbances from the noise term $\vec{P}$ are also small. We can determine this simply from the eigenvalues of the system. As the Jacobian matrix is not symmetric we decompose it with left $\mathcal{L}$ and right $\mathcal{R}$ eigenvector matrices

$$\begin{aligned} \mathcal{J}\mathcal{R} &= \mathcal{R}\ \mathrm{diag}(\lambda_n), \\ \mathcal{L}\mathcal{J} &= \mathrm{diag}(\lambda_n)\ \mathcal{L} \\ \mathcal{L}\mathcal{R} &= \mathrm{diag}(e_n), \end{aligned} \tag{30}$$

with $n = 1, \ldots, 14$ eigenvalues λ_n and normalizing values e_n. Stability is now guaranteed if all eigenvalues have a real part $\mathrm{Re}\,\lambda_n < 0$. In our case this depends not only on the parameter set, but also on the wave number value $\vec{k}^2$ in Eq. (29). We found that for the 27 parameter sets investigated in the previous subsection, $\mathrm{Re}\,\lambda_n < 0$ for *all* $\vec{k}^2$. In this sense then a linear approximation of those sets is viable.

We can however go one step further and predict the power spectrum from our eigendecomposition. Using a Fourier transform in time of Eq. (28) with $\vec{s}(\vec{k},t) \to \vec{s}(\vec{k},\omega)$ and Eq. (30)

$$\begin{aligned} i\omega\vec{s} &= \mathcal{J}\cdot\vec{s} + \vec{P}, \\ \mathrm{diag}(i\omega - \lambda_n)\cdot\mathcal{L}\cdot\vec{s} &= \mathcal{L}\cdot\vec{P}, \\ \vec{s} &= \mathcal{R}\ \mathrm{diag}\left[\frac{1}{e_n(i\omega - \lambda_n)}\right]\cdot\mathcal{L}\cdot\vec{P} \equiv \mathcal{P}\cdot\vec{P}. \end{aligned} \tag{31}$$

In the last step we have assumed that $\mathcal{R}$ forms a basis $\vec{s} = \mathcal{R}\cdot\vec{s}_{\mathcal{R}}$ and that $e_n(i\omega - \lambda_n) \neq 0$. In this paper we are primarily concerned with the first component $s_1(\vec{k},\omega) = h_e(\vec{k},\omega)$ and $\vec{P}$ is zero except for its fourth component. Hence here we only need to compute the component $\mathcal{P}_{14}$ in order to predict the power spectrum. Furthermore our input noise in $\vec{P}_4$, as well as $\mathcal{P}$, depends only on the magnitude $k = |\vec{k}|$, so we can write

$$|h_e(k,\omega)|^2 = |\mathcal{P}_{14}(k,\omega)P_4(k,\omega)|^2 \propto |\mathcal{P}_{14}(k,\omega)|^2. \tag{32}$$

The final proportionality applies only for $\omega/(2\pi) \lesssim 50$ Hz and $k/(2\pi) \lesssim 1.75\ \mathrm{cm}^{-1}$, where our noise input is unfiltered and hence $P_4(k,\omega)$ is constant in Fourier space.

If we wish, we can now predict the power spectrum for specified k modes. Indeed, we find that all spectra of Fig. 6 are fairly well fitted by using a common $k \simeq 1.24\ \mathrm{cm}^{-1}$. Note that this is much smaller than the onset of filter suppression at $k \simeq 11\ \mathrm{cm}^{-1}$. The evaluation of Eq. (32) with a fixed wave number is extremely rapid, and the overall good fit with $k \simeq 1.24\ \mathrm{cm}^{-1}$ suggests an average dominant wavelength of around 5 cm for these sets. However, this value is not universal (see the discussion of Fig. 7 below), and it becomes particularly problematic to assume so in the investigation of anesthesia. It is *a priori* neither clear that one can find a typical wavelength in the anesthetized state nor what value it may have.

Instead we can consider an integration over a fixed size spatial patch, in analogy to the way EEG electrodes sum up

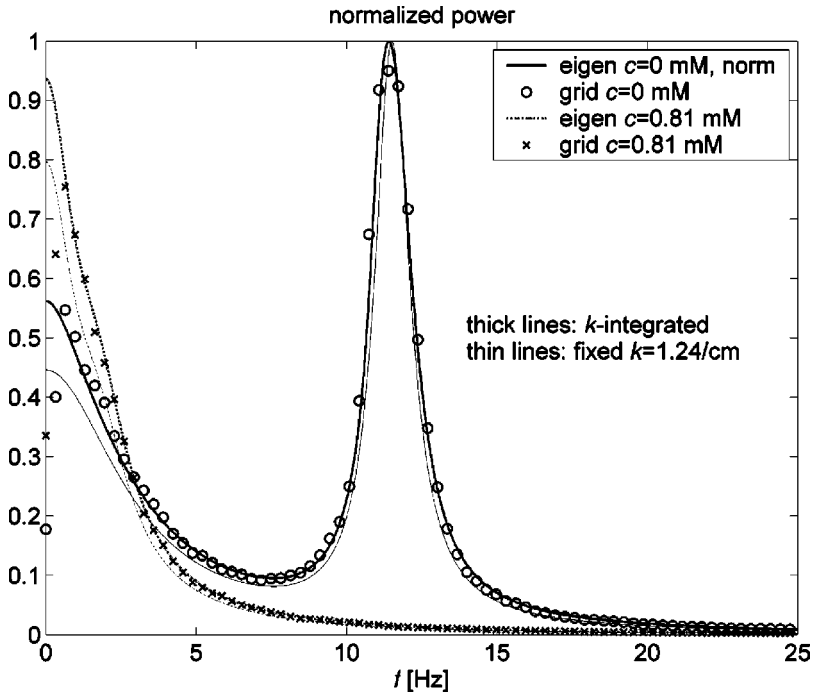

FIG. 7. Normalized eigenspectra using Eq. (38) as thick and Eq. (32) with $k=1.24\ \mathrm{cm}^{-1}$ as thin lines, respectively, in comparison with the average power spectra (3.072 s, detrended, Hanning window) from the grid with Table III parameters.

the signal of a patch of cortex. The total potential measured at position $\vec{x}$ with $\vec{x},\vec{x}' \in \mathbb{R}^2$ is

$$\phi(\vec{x},\omega) = \int d^2x' \Psi(\vec{x}' - \vec{x}) h_e(\vec{x}',\omega), \tag{33}$$

$$\phi(\vec{k},\omega) = \int d^2x\, e^{-i\vec{k}\cdot\vec{x}} \phi(\vec{x},\omega) = \Psi(-\vec{k}) h_e(\vec{k},\omega), \tag{34}$$

where $\Psi(\Delta\vec{x})$ represents the weight of a contribution at distance $\Delta\vec{x}$. The total power spectrum is then

$$H(\omega) = \int d^2x |\phi(\vec{x},\omega)|^2 = \frac{1}{(2\pi)^2} \int d^2k |\phi(\vec{k},\omega)|^2. \tag{35}$$

The simplest assumption is that contributions come only from a two-dimensional disk of radius R and there with equal weight

$$\Psi(\Delta\vec{x}) = \Psi(|\Delta\vec{x}|) = \begin{cases} 1 & \text{for } |\Delta\vec{x}| \leqslant R, \\ 0 & \text{otherwise}, \end{cases} \tag{36}$$

$$\Psi(\vec{k}) = \Psi(k) = \frac{2\pi R}{k} \mathrm{J}_1(kR), \tag{37}$$

where J_1 is a Bessel function of the first kind. If h_e also depends only on the magnitude k as in Eq. (32), we can reduce Eq. (35) to

$$H(\omega) = 2\pi R^2 \int_0^\infty \frac{dk}{k} \mathrm{J}_1^2(kR) |h_e(k,\omega)|^2. \tag{38}$$

Note that for $|h_e(k,\omega)|^2 = \text{const}$, $H(\omega) = \pi R^2 \times \text{const}$. We chose $R=0.77$ cm in the following, which gives a realistic sample area of almost 2 cm^2 [1]. Note that the infinite upper limit for the integration does not pose a numerical problem. Our choice of spatial noise filter means $P_4(k > 14.14\ \mathrm{cm}^{-1},\omega)=0$ and hence the integral in Eq. (38) is definite in practice.

In Fig. 7 we show the quality of the "eigenspectrum" estimate in comparison with average spectra from a full grid simulation. The agreement is impressive. Thus the frequency content of the grid output is relatively independent of the grid geometry and of the input noise distribution for small enough δp_{ee} {grid $\mathcal{N}[n(\overline{p_{ee}},\delta p_{ee}),\vec{x},t] \rightarrow$ "eigenspectrum" $\overline{p_{ee}}$}. Note that the apparent disagreement at $\lesssim 1.3$ Hz is an artifact of the detrending and finite length of the time series. The "eigenspectra" shown have been estimated using Eq. (38). If instead one uses a fixed $k = 1.24\ \mathrm{cm}^{-1}$ and Eq. (32), as before, one obtains a slightly shifted α peak with smaller frequency width, as well as reduced δ activity. This prediction is shown by the thin lines in Fig. 7 and obviously diagrees somewhat with the results from our grid simulation. Apparently then, the dependence of $h_e(k,\omega)$ on k is appreciable for the parameter set of Table III. One can usually find a fixed k that matches the corresponding grid results well, but that scale is not universal. In Fig. 7 we also show the prediction for a fully anesthetized state (3.33 MAC isoflurane), just as in Fig. 4. The integrated eigenspectrum prediction continues to be in excellent agreement, whereas the one for fixed k still falls short.

E. Pole sensitivity

The linearization of Eqs. (1)–(6) and (12) also enables the semianalytical determination of the sensitivity of our model resonances to parametric perturbations induced by GAs based on our current knowledge regarding their targets of action. Because the linearized behavior of our theory depends dominantly on the location in the complex plane of the corresponding poles, it is sufficient to investigate their mo-

TABLE III. Parameters within the ranges of Table I yielding a physiological power spectrum, Figs. 4(b) and 7, appropriate firing rates, Fig. 5, and a stable "biphasic" power surge under anesthesia, Fig. 9.

h_e^r	−62.226 mV	h_i^r	−65.666 mV
τ_e	132.55 ms	τ_i	135.91 ms
h_{ee}^{eq}	−18.038 mV	h_{ei}^{eq}	−16.554 mV
h_{ie}^{eq}	−81.976 mV	h_{ii}^{eq}	−78.995 mV
Γ_{ee}	0.10631 mV	Γ_{ei}	0.64105 mV
Γ_{ie}	0.46477 mV	Γ_{ii}	0.28663 mV
γ_{ee}	291.50 s^{-1}	γ_{ei}	697.76 s^{-1}
γ_{ie}	458.67 s^{-1}	γ_{ii}	82.330 s^{-1}
N_{ee}^{β}	2185.8	N_{ei}^{β}	3749.8
N_{ie}^{β}	466.30	N_{ii}^{β}	160.69
N_{ee}^{α}	4611.6	N_{ei}^{α}	1372.4
$\Lambda_{(ee=ei)}$	0.92809 cm^{-1}	v	684.24 cm/s
$S_e^{\max}$	196.08 s^{-1}	$S_i^{\max}$	454.40 s^{-1}
$\overline{\mu_e}$	−45.104 mV	$\overline{\mu_i}$	−43.910 mV
$\hat{\sigma}_e$	3.8420 mV	$\hat{\sigma}_i$	4.5793 mV
$\overline{p_{ee}}$	6603.4 s^{-1}	δp_{ee}	660.34 s^{-1}
p_{ei}	2625.7 s^{-1}	$p_{ie,ii}$	0 s^{-1}
ξ	0 ms	r_{abs}	0 ms

tion in response to such parametric perturbations.

The first component of Eq. (31) can be written in transfer function form as

$$h_e(k,\omega) = \frac{N(\omega,\vec{q},x_e)}{D(\omega,\vec{q},x_e)} P_4(k,\omega), \tag{39}$$

with $\mathcal{P}_{14}=N/D$. The notation with $\vec{q}$ and x_e makes explicit the dependences of the model: $\vec{q}$ consists of the independent parameters listed in Table I and of the wave number k, and x_e represents the singular point around which we linearize. To obtain x_e Eq. (18) is inserted into Eq. (19) and then an equation of the form $F(x_e,\vec{q})=0$ is solved with a chosen $x_e^*(\vec{q})$.

The total derivative of this equation with respect to q_j at $x_e^*(\vec{q})$ is

$$\frac{\delta F}{\delta q_j}[x_e^*(\vec{q})] = \left[\frac{\partial F}{\partial x_e}\frac{\partial x_e}{\partial q_j} + \frac{\partial F}{\partial q_j}\right]_{x_e^*} = 0. \tag{40}$$

In order to determine the poles we solve $D(\omega,\vec{q},x_e)=0$ for ω. For a specific pole $\omega^*(\vec{q},x_e)$ we similarly obtain the total derivative of the equation

$$\frac{\delta D}{\delta q_j}[\omega^*(\vec{q},x_e)] = \left[\frac{\partial D}{\partial \omega}\frac{\partial \omega}{\partial q_j} + \frac{\partial D}{\partial x_e}\frac{\partial x_e}{\partial q_j} + \frac{\partial D}{\partial q_j}\right]_{\omega^*} = 0. \tag{41}$$

The sensitivity of a model pole ω^* to a normalized change $\hat{q}_j=(q_j-q_j^*)/q_j^*$ around the given parameter set $\vec{q}^*$ is then found by substituting Eq. (40) into Eq. (41),

$$\frac{\partial \omega^*}{\partial \hat{q}_j} \equiv \frac{\partial q_j}{\partial \hat{q}_j}\left[\frac{\partial \omega}{\partial q_j}\right]_{x_e^*,\omega^*} = q_j^* \left[\frac{\dfrac{\partial D}{\partial x_e}\dfrac{\partial F}{\partial q_j} - \dfrac{\partial D}{\partial q_j}\dfrac{\partial F}{\partial x_e}}{\dfrac{\partial F}{\partial x_e}\dfrac{\partial D}{\partial \omega}}\right]_{x_e^*,\omega^*}. \tag{42}$$

$\mathrm{Re}[\partial\omega^*/\partial\hat{q}_j]$ and $-\mathrm{Im}[\partial\omega^*/\partial\hat{q}_j]$ give the sensitivities of angular frequency and damping, respectively. It is perhaps helpful to note that the pole and its corresponding eigenvalue relate as $\mathrm{Re}\,\omega^*=\mathrm{Im}\,\lambda^*$ and $\mathrm{Im}\,\omega^*=-\mathrm{Re}\,\lambda^*$. The evaluation of the expressions in Eq. (42) generally requires a symbolic algebra program.

Now the predicted change in the EEG resonant frequency, $\Delta\omega^*$, for *small* normalized changes in the parameters $\Delta\hat{q}_j$ simply becomes

$$\Delta\omega^* = \sum_j \frac{\partial \omega^*}{\partial \hat{q}_j}\Delta\hat{q}_j. \tag{43}$$

On the basis of our current understanding of the subcellular targets of inductive GA action (e.g., isoflurane) we can hypothesize that dominantly

$$\Delta\omega^* = \frac{\partial \omega^*}{\partial \hat{\gamma}_{ie}}\Delta\hat{\gamma}_{ie} + \frac{\partial \omega^*}{\partial \hat{\gamma}_{ii}}\Delta\hat{\gamma}_{ii}, \tag{44}$$

which expresses the fact that the principal effect of GAs at low concentrations is to increase charge transfer at inhibitory synapses, i.e., $\Delta\hat{\gamma}_{ii},\Delta\hat{\gamma}_{ie}<0$; see also Fig. 2(d). A similar hypothesis can be postulated for dissociative GAs (e.g., ketamine) assuming that at low concentrations they primarily reduce charge transfer at excitatory synapses: $\Delta\hat{\Gamma}_{ee},\Delta\hat{\Gamma}_{ei}<0$.

V. SIMULATION RESULTS

A. Average behavior of parameter sets

In the following we will be employing exclusively the linear approximation in the search for reasonable power spectra in parameter space. This has the obvious disadvantage that we will overlook all nonlinear solutions. However, it appears that linear solutions are much more common and cover the observed range of real human power spectra. Indeed spontaneous EEGs recorded with and without the presence of GAs are generally indistinguishable from a linear random process (see Sec. VI for further details). The huge advantage of the linear approximation is simply computational speed. On a typical personal computer we can evaluate the eigenspectra of 10^5 parameter sets in less than 1 min. That includes all the varied tests we perform in order to determine whether the spectrum is of reasonable shape. With this kind of speed it becomes possible to search the parameter space with Monte Carlo methods. Depending on the details of our selection criteria, we find one proper solution in about every 10^5 trials.

Given a randomly generated set of parameters, we first check that a singular point solution exists which implies inhibitory and excitatory firing rates between 0.1 and 20 s^{-1}.

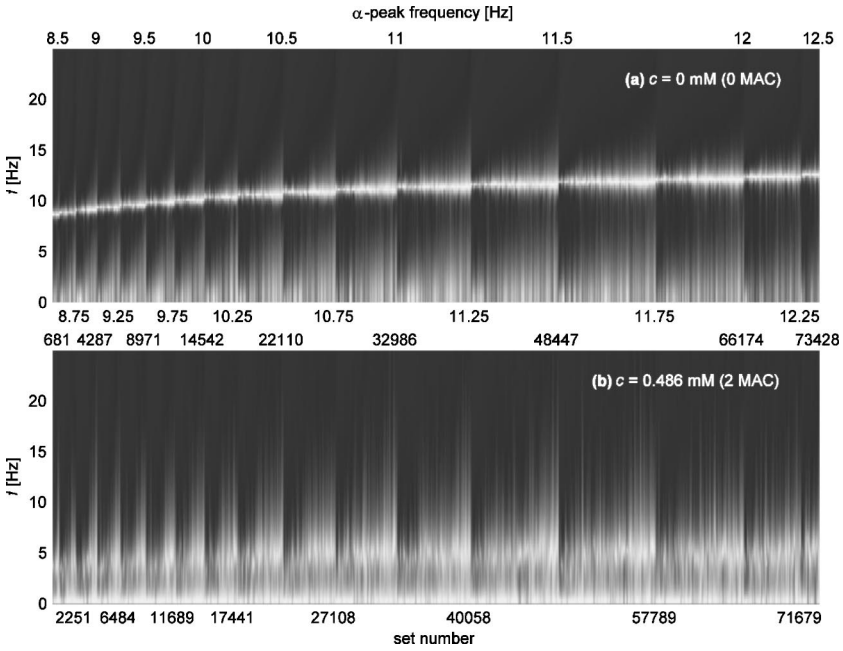

FIG. 8. (a) Eigenspectra of 73 454 "linear" parameter sets. The spectra are displayed along the vertical axis at 0.25 Hz frequency resolution with gray scale indicating their normalized values ($0 \leftrightarrow$ black to $1 \leftrightarrow$ white). The spectra are sorted along the horizontal axis according to their α-peak frequency. (b) Corresponding eigenspectra at 2 MAC isoflurane; the order along the horizontal axis from (a) has been maintained, but now set numbers are shown. Example: there are 2853 eigenspectra with 10 Hz α peak frequency ["9.75" to "10" in (a), "11 689" to "14 542" in (b)].

Second, we check that the solution is stable $\forall\, \mathrm{Re}\,\lambda_n < 0$. Then we compute the eigenspectrum. The third test is on the power in the δ (0–4 Hz), θ (4–8 Hz), α (8–13 Hz), and β (13–30 Hz) bands. The criteria used have undergone some variations and viable solutions have been retained throughout. About half the solutions come from a selection run which required 15–50 % of total power in δ, 10–25 % in θ, 15–40 % in α, 15–40 % in β, and power ratios $\theta/\delta < 0.6$ and $\theta/\alpha < 0.7$. Fourth, we check the 90% spectral edge frequency (SEF_{90}), which is defined as the frequency below which 90% of the power resides. In the mentioned selection run SEF_{90} was required to be 12–21 Hz. Fifth, we compute the quality of the α peak by subtracting background linearly and requiring $Q = \Delta f_\alpha / f_\alpha > 5.5$, where Δf_α is the full width at half maximum. Sixth, we look at the extremal values of the spectra in the δ, θ, and α bands. Here we require that the α maximum is not larger than five times and not smaller than one-third the δ maximum. Furthermore, the θ minimum may not be larger than half of either the α or δ maxima, and not larger than 90% of the δ minimum.

The final, seventh test concerns the behavior with regard to anesthesia. Here we go from zero to 3.33 MAC isoflurane in 30 steps and check that the solution remains stable throughout, as clinical experience indicates that isoflurane induces seizures only very rarely (see for example Ref. [43]). This involved procedure is necessary in a completely automated search to suppress spectra which appear unreasonable to the trained human eye: the remaining spectra look like typical "occipital α" EEGs and compare well with human spectra recorded by our group. However, our criteria do not represent an attempt to characterize the full range of such human EEGs, but simply aim to select a sufficiently representative sample.

In Fig. 8 we display the final result: 73 454 spectra generated from as many parameter sets as have survived the cuts. As mentioned above, these sets have been selected from roughly 7×10^9 randomly generated parameter sets and it took the equivalent of 52 days on a single PC to obtain these solutions. Since we were able to use a PC cluster, the bare computation was performed in less than two days. However, considerable extra time was spent on optimizing the selection process. Although solutions with larger α frequency appear more common, this does mainly reflect the mentioned selection rules for about half of the solutions. There we forced the power in the β band to be comparatively high, which is more readily satisfied with an α resonance at higher frequencies. Figure 8 also shows how these spectra change under anesthesia. There is a clear shift of the former α band toward lower frequencies. At the shown 2 MAC isoflurane the gap to the δ band has almost closed. Furthermore, we observe a general tendency of the former α peak to broaden considerably.

By calculating the linear sensitivity of these sets to GA-induced parametric perturbations we can evaluate the ability of our theory to account for the most general EEG features of the GA effect. Table IV shows calculated sensitivities for the two most weakly damped poles of Eq. (39) in response to small perturbations in a range of parameters expected, on the basis of experimental evidence, to be modified by GAs. We have averaged over 86 sets chosen at random from the 73 454 and set $k = 1.24\ \mathrm{cm}^{-1}$. As discussed in Sec. IV E it is reasonable to assume that $\Delta\hat{\gamma}_{ii}, \Delta\hat{\gamma}_{ie} < 0$ describes inductive GA action at low concentrations. If we further assume, to first order, $\Delta\hat{\gamma}_{ie} = \mu\Delta\hat{\gamma}_{ii}$ then we are able to conclude [see Eq. (44)] that if $0 < \mu \lesssim 7.7$ then inductive GAs will be associated with a reduction in the frequency and damping (i.e., $\mathrm{Re}\,\Delta\omega^* < 0$, $-\mathrm{Im}\,\Delta\omega^* > 0$) of the α pole. μ can be identified with the relative efficacy of the GA at inhibitory synapses on excitatory cells compared to inhibitory synapses on inhibitory neurons. To our knowledge no experimental evidence exists for $\mu \neq 1$.

Thus the effects of low concentrations of GA are qualitatively predicted to be associated with a change to higher-amplitude, lower-frequency EEG activity. This prediction is in accord with experiment and the known proconvulsant

TABLE IV. Sensitivity to normalized parameter changes of the frequency and damping of the two most weakly damped poles averaged over 86 randomly chosen sets ($k=1.24\ \mathrm{cm}^{-1}$). One of the poles (a conjugate pair) has α frequency, the other $\simeq 0$ Hz. The frequency sensitivity of the latter is negligible.

	Sensitivity (rad/s)		
	Frequency $\mathrm{Re}(\partial\omega^*/\partial\hat{q}_j)$	Damping $-\mathrm{Im}(\partial\omega^*/\partial\hat{q}_j)$	
Normalized change of parameter $\hat{q}_j$	α	α	$\simeq 0$ Hz
$\hat{\Gamma}_{ee}$	32.5	8.2	−7.3
$\hat{\Gamma}_{ei}$	4.4	1.8	−2.8
$\hat{\Gamma}_{ie}$	−19.0	−1.6	−3.4
$\hat{\Gamma}_{ii}$	17.4	1.1	2.8
$\hat{\gamma}_{ee}$	−32.4	−8.2	6.2
$\hat{\gamma}_{ei}$	−1.8	−2.9	2.8
$\hat{\gamma}_{ie}$	23.3	0.7	4.2
$\hat{\gamma}_{ii}$	16.5	−5.4	−8.8

properties of a range of volatile GAs. Because sensitivities of pole damping for the zero-frequency case have approximately the same magnitude but opposite signs for equivalent changes in $\Delta\hat{\gamma}_{ie}$ and $\Delta\hat{\gamma}_{ii}$ we would expect it to contribute little to changes in total EEG power at low anesthetic concentrations. Since dissociative anesthetic agents like ketamine or xenon are assumed to principally reduce Γ_{ee} and Γ_{ei} their predicted effect, at low concentrations, is to reduce the frequency, and increase the damping, of the α pole. Thus, qualitatively at least, inductive and dissociative GAs are predicted to have different effects on electroencephalographic stability. At low concentrations dissociative GAs promote cortical stability, whereas inductive GAs promote cortical instability.

However, to obtain quantitative predictions one should take into account all poles and their respective gains. Thus we turn again to the full expression given by Eqs. (31), (32), and (38). In order to elucidate the general trends for changing concentrations of an anesthetic agent, we now compute a number of quantities for all 73 454 sets and concentrations from 0 to 3.33 MAC: the total power at c relative to the total power at zero concentration; the fraction of power residing in δ, θ, α, β, and γ bands; and the spectral edge frequencies below which 50%, 90%, and 95% of all power resides. These quantities are shown by the light shaded bands in Fig. 9, as computed from the eigenspectra of the sets. The edges of the bands represent the 16% and 84% quantiles of the distribution of values at a particular c. The middle line represents the median, i.e., the 50% quantile. Thus 68% of the 73 454 sets have a value within the shown band.

As anesthetic concentration increases, for most sets total power decreases. The fraction of power in δ and θ is above baseline at high concentrations. The fraction of δ power first rises and then falls mildly at lower concentrations, before steadily increasing. In contrast θ power rises quickly at lower concentrations and then slowly sinks again. At the same time the fraction of power in the α and β bands steadily falls. All this is consistent with the motion of the original α pole toward lower frequencies.

It is interesting to see that power in the γ band is not on average diminishing, and hence also the spectral edge frequencies at 90% and 95% remain fairly steady. The combination of slowly falling β and steady γ fractions of power suggest that the former α peak is becoming broader while moving to lower frequencies. On the other hand, SEF_{50} is falling as one may have expected. Since the SEF_{50} frequency is in the α range, it traces directly the shift of the α peak. The results shown are consistent with what we expect from the

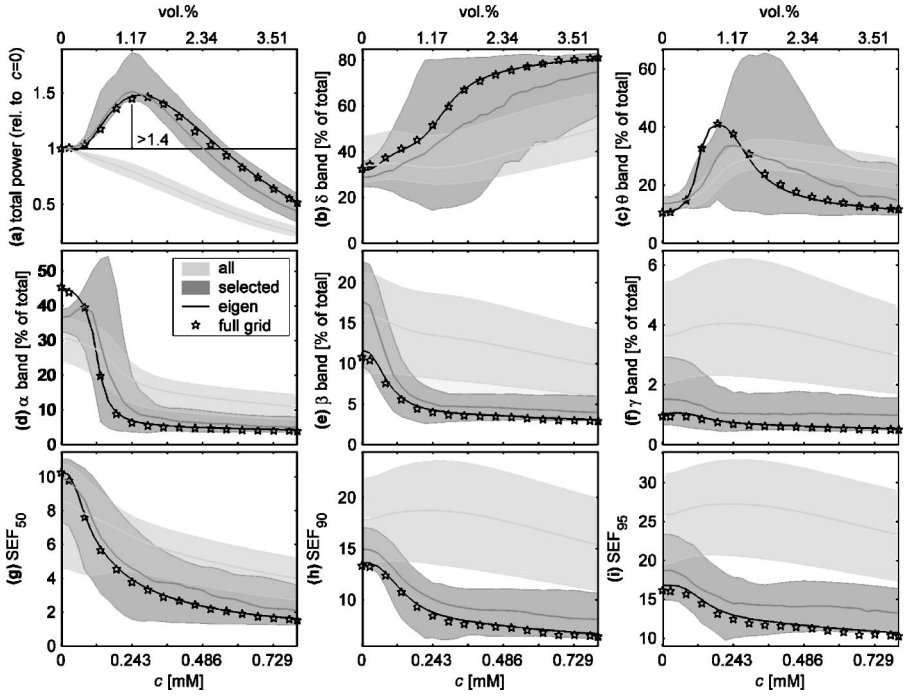

FIG. 9. The bands display the 16% (lower edge), 50% median (middle line), and 84% (upper edge) quantile of all 73 454 (light) and 86 selected (dark) parameter sets. The selection criterion is marked in (a). Results for the set of Table III, one of the 86, are shown by a solid black line (eigenspectrum) and stars (grid simulation). The plots show the following variable's dependence on isoflurane concentration c: (a) total (0–60 Hz) power normalized to that at $c=0$ mM; (b) δ (0–4 Hz), (c) θ (4–8 Hz), (d) α (8–13 Hz), (e) β (13–30 Hz), (f) γ (30–60 Hz) fraction of power; (g) 50% median, (h) 90%, (i) 95% spectral edge frequency.

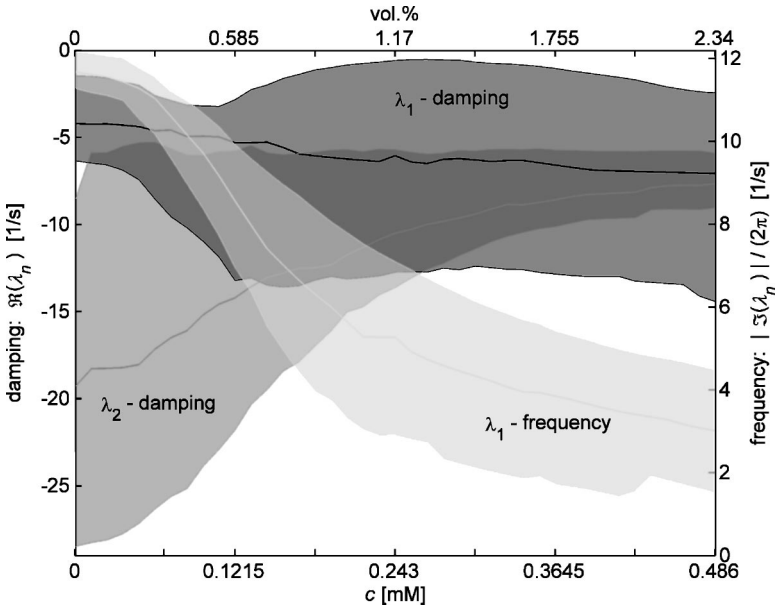

FIG. 10. Bands (16–84 % quantile, middle line is median) showing the change with isoflurane concentration for the two least damped eigenvalues. Frequency $|\mathrm{Im}(\lambda_2)|/(2\pi)=0$ for all 86 "biphasic" sets used.

pole movement predictions, but we do not see the expected "biphasic" behavior of total power in the shown 68% of the 73 454 sets. That is to say, we do not see total power first rise and then fall with concentration of the anesthetic agent. Also, SEF_{90} and SEF_{95} are expected to fall with higher concentrations of anesthetic agent. However, if we take a look at the parameter set of Table III, which we have already analyzed in Figs. 4, 5, and 7, a different picture emerges. In Fig. 9 the solid black line represents the predictions from its eigenspectra. The stars in the same plot represent the predictions obtained from the full grid run. The grid power spectrum has been corrected for the missing power below 1.3 Hz (see the discussion of Fig. 7) by replacing it there with its corresponding eigenspectrum.

First, once more we find very good agreement between full grid and eigenspectra predictions for all concentrations of anesthetic agent. Second we note that for this particular set, which is one of the 73 454, we do obtain a "biphasic" power rise and we also see that for this set SEF_{90} and SEF_{95} fall similarly to SEF_{50}. This suggests applying a further cut on our sets to select only those with such a "biphasic" power rise. These sets are obviously to be found in the 32% of sets not represented in the light shaded total power band.

B. Sets selected for "biphasic" behavior

At 1 MAC isoflurane ($c=0.243$ mM) we require total power to have risen at least to 1.4 times its values at $c=0$ mM. Out of the 73 454 sets, this selects a mere 86—including the one of Table III. The quantiles computed from only these selected sets are displayed in Fig. 9 as dark shaded bands. The desired "biphasic" change of total power has been obtained. But without any further tuning, ameliorated behavior of SEF_{90} and SEF_{95} also follows. Obviously, this is reflected in the fraction of power in the γ band. There is also an enhanced rise and fall in θ fractional power and greater variability of the behavior there and in the δ band, which now shows a steady increase of the median. For the 86 selected sets the power fraction in the α band now remains steady or even rises at low concentrations, before falling rapidly at higher concentrations. The fall in β is now considerably faster. This suggests an α pole which initially moves only slowly toward lower frequencies and does not broaden quickly.

In order to confirm this, Fig. 10 traces the motion of the two least damped eigenvalues λ_1 and λ_2 with changing GA agent concentration up to 2 MAC isoflurane ($c=0.486$ mM). The bands represent the 16%, 50% (middle line), and 84% quantiles of the the 86 "biphasic" sets. $\mathrm{Re}(\lambda_n)<0$ yields the damping and $|\mathrm{Im}(\lambda_n)|/(2\pi)$ the frequency of the eigenvalue. $\mathrm{Im}(\lambda_2)=0$, i.e., the second least damped eigenvalue is always real. All other eigenvalues are so strongly damped that they play only a marginal role. We see that the least damped eigenvalue λ_1 (actually a conjugate pair of eigenvalues) has a frequency mainly in the medium to high α range. As concentration increases, this frequency at first stays roughly the same, but then decreases quickly to θ and finally δ frequencies. Around 0.5 MAC the median of λ_1 frequencies drops out of the α band. Consequently we see in Fig. 9 a sudden decrease in the fraction of α power and an increase in the fraction of θ power around this concentration.

The slow and roughly linear *increase* in median damping of λ_1, i.e., broadening of the associated peak in the power spectrum, coincides at first with the peak moving more completely into the α band. In Fig. 9 we see an initial increase in the median α fraction and loss in the median β fraction of power. The edges of the λ_1 damping band show more structure. For example, just before 0.5 MAC a *decrease* in least damping (upper edge of band) of λ_1—sharpening of some α peaks—results in an increase in the highest fraction of α power (upper edge of band) considerably above baseline in Fig. 9. However, the median λ_1 peak still broadens as it moves into the θ band. Around 1 MAC the combination of broadening and motion to lower frequencies starts to seriously leak power from θ into δ, and the median peak itself crosses into θ at around 1.4 MAC. The other eigenvalue λ_2

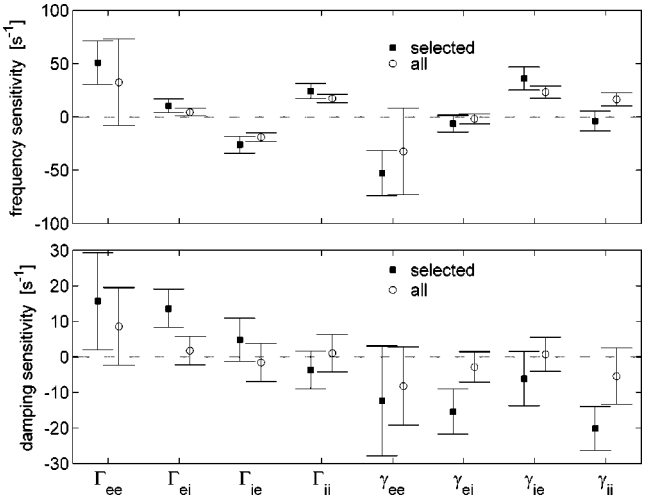

FIG. 11. Mean and standard deviation of the α pole frequency (Re $\partial\omega^*/\partial\hat{q}_j$) and damping ($-$Im $\partial\omega^*/\partial\hat{q}_j$) sensitivities of 86 parameter sets which showed a strong "biphasic" response, in comparison to 86 others which did not (see Table IV). Differences in means were uniformly highly significant with $p \ll 0.001$, except for γ_{ee} damping, as determined by a large sample distribution-free method [44].

in Fig. 10 shows a steady *decrease* in damping, which slows down at higher concentrations. This sharpening of the λ_2 peak corresponds to a continuous increase in the median δ fraction of power in Fig. 9.

It is interesting to note that the local sensitivity analysis of Sec. IV E by itself is sufficient to distinguish α parameter sets that show a demonstrable surge in power (the "biphasic" response) as a function of anesthetic concentration, from those that do not. Figure 11 compares the pole sensitivities obtained for the 86 sets selected here with the 86 parameter sets previously selected at random to represent all 73 454 plausible sets. The results for the latter are collected in Table IV. None of the 86 "biphasic" parameter sets are also included in the random selection.

The differences in the means, for all parameter sensitivities except γ_{ee} damping, between the two sets are uniformly highly significant $p \ll 0.001$ with a large sample distribution-free method [44]. It is notable that changes in $\Delta\hat{\gamma}_{ii}$ and $\Delta\hat{\gamma}_{ie}$ no longer have opposing effects on α pole damping for the "biphasic" sets. Further the magnitude of these sensitivities is augmented. Thus the sensitivity profile of the "biphasic" sets may become a principal determinant for the expectation of GA-induced EEG power surges at anesthetic concentrations generally associated with LOC. Experimentally this may enable studying the effects and mechanisms of GA at low concentrations.

From a more technical point of view these differences imply that there are additional physiological constraints on the parameters which are not explicitly incorporated yet in our parameter searches. This is also indicated by the very low yield of acceptable power spectra and firing rates, and even lower yield of "biphasic" behavior, from randomly generated parameter sets. Future experimental data may tighten the ranges in Table I, thereby ameliorating the situation. But it is reasonable to assume that natural variations in one parameter will require compensatory changes in others to keep the brain functional.

Thus high yields can only be expected from appropriately *correlated* variations of model parameters. Unfortunately, at this point in time little external information about such correlations is available. Furthermore, correlation patterns in high-dimensional parameter spaces are hard to discern, in particular with a still very small number of sample points per dimension. A thorough scan is currently infeasible: ten steps per dimension yields 10^{32} evaluations, or about 2×10^{21} PC years. Since, however, our completely random search assumes no correlations, we can interpret the differing sensitivities of "biphasic" sets as unbiased evidence for such expected correlations. More results like these are needed to constrain and improve the model. Nonetheless, our successes so far suggest that the basics of the model are sound.

VI. CONCLUSIONS

Two general approaches have distinguished themselves in accounting for the effects of GAs on neural activity. The first kind employs spatially discrete network models of neurons with a variety of voltage- and ligand-dependent ionic conductances. Although useful *per se* [17], it is nevertheless difficult to relate the resulting dynamics of such models to clinically measurable macroscopic effects—like the EEG. The second kind of modeling approach seeks to link the known microscopic targets of GA action with their macroscopic effects through mean field spatially continuous approaches.

To our knowledge only two other works utilizing this kind of approach can be identified previous to this paper. The first, by Steyn-Ross *et al.* [6], modeled GA action as a first order phase transition, induced by an order parameter dependent on GA concentration. Their calculations take the same starting point as ours, Eqs. (1)–(6) of Liley *et al.* Thus in a sense our approach can be seen as the next evolutionary step of the same mean field method. However, despite these fundamental similarities they find qualitative agreement with observed GA effects on the EEG only under physiologically implausible circumstances. We will come back to this related model in more detail below. The second, by Ting *et al.* [7], attempted to describe the effects of GAs on evoked cortical responses (ECRs) based on the theoretical works of Freeman [45] and Rotterdam *et al.* [46]. While being able to model the progressive attenuation of amplitude and prolonged latency of ECRs seen with increasing agent concentration, it did so without incorporating any of the currently identified GABAergic targets implicated in inductive GA action.

In this paper we have addressed the mentioned shortcomings of both previous works. We have shown that the observed spectral features of the human EEG, and in particular their response to GAs, can be successfully accounted for using a physiologically parametrized, spatially continuous mean field formulation of electrocortical neurodynamics. Furthermore, by developing a different approach to parametrizing the action of anesthetic agents we were able to incorporate into our macroscopic model detailed and specific experimental data for the stereotypical inductive GA isoflurane concerning its effects on IPSP and EPSP amplitudes and

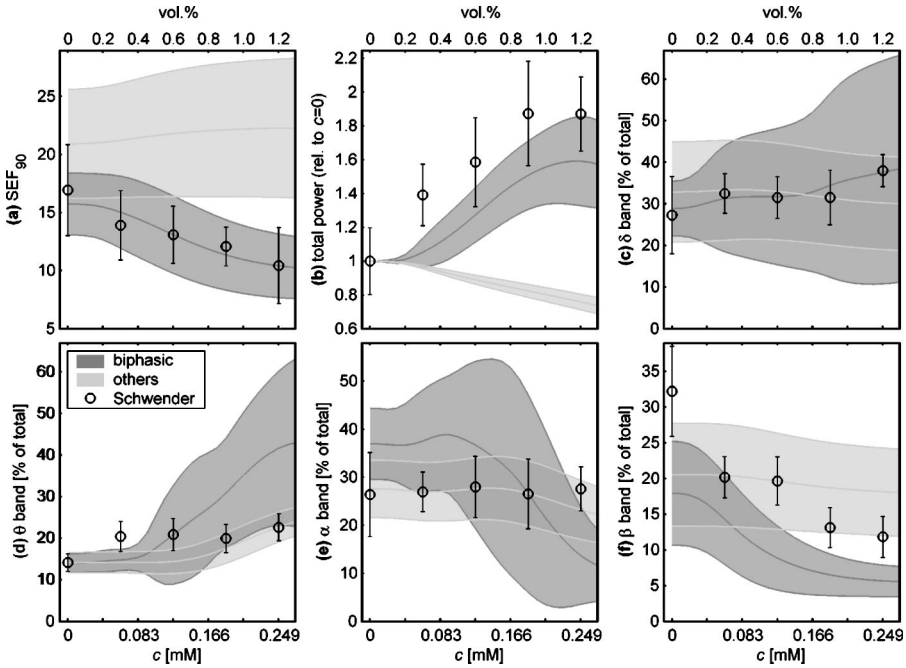

FIG. 12. Comparison of the means and standard deviations of (a) SEF_{90}, (b) total power normalized to that at $c=0$ mM, (c) δ, (d) θ, (e) α, and (f) β band fraction of power of data from 12 patients in Schwender *et al.* [54] (error bars) with eigenspectra predictions from 12 parameter sets each in Table V (dark bands) and Table VI (light bands), respectively. The parameter sets have been chosen to match the data better than a random selection would, but do not represent a proper fit.

time courses. While the full theory consists of a coupled set of eight nonlinear, two-dimensional partial differential equations, almost all physiologically plausible behavior could, somewhat remarkably, be obtained from a linear analysis about the system's low firing singular points. This was verified by comparing with parallelized computer simulations of the complete theory on grids representing the full typical spatial extent of human cortex.

Our conclusion that the resting EEG, and its behavior during anesthesia, can be modeled as a linear random process is in accord with the results of a number of nonlinear dynamical analyses of experimental data. For instance Stam *et al.* [47] used nonlinear forcasting techniques in conjunction with surrogate data testing to investigate the prevalence of α rhythm nonlinearity in resting EEGs. Out of 480 2.5 s EEG epochs, obtained from 60 healthy male and female participants, only 6 (1.25%) could be distinguished from linearly filtered white noise using these methods. The successful use of bispectral measures (BIS monitoring) in determinations of anesthetic depth would seem to suggest that this conclusion may not be valid for EEGs recorded in the presence of GAs. The bispectrum and its normalized version, the bicoherence, are used to detect nonlinearities such as interfrequency phase coupling [48].

However, recent detailed analyses of EEGs recorded from patients undergoing some form of surgery suggest that such an EEG, like its resting counterpart, is indistinguishable from filtered white noise. Specifically Schwilden and Jeleazcov [49] analyzed 26.4 h of EEGs recorded from a total of eight patients undergoing abdominal sugery. They found that the fraction of epochs for which a nontrivial bicoherence was detected was 6.2%, compared with 13.8% obtained using synthetic Gaussian (white noise) data. Supporting the relevance of this result, Miller *et al.* [50], on the basis of clinical comparisons, were unable to show that a bispectral analysis was any better than a power-spectral-based analysis in characterizing the anesthetic state.

By studying the theory's defining equations in linear approximation, we were able to rapidly search its large and complex multidimensional parameter space. This allowed us to find physiologically relevant parametrizations which exhibit the typical features of the human EEG power spectrum in the δ, θ, α, and β bands, as well as reasonable mean firing rates. Starting from such "normative" EEG behavior, we were then able to meaningfully study its modulation in response to the systematic changes in inhibitory and excitatory neurotransmission induced by GAs. A parameter sensitivity analysis around zero concentration showed that, on average, inductive GAs like isoflurane reduce the damping and frequency of the conjugate pair of poles constituting the α resonance. Such behavior is qualitatively consistent with the known GA effect of shifting EEG power from a high-frequency, low-amplitude state to a low-frequency, high-amplitude one.

We then went on to calculate the quantitative behavior of our theory over GA concentrations typically needed to induce and maintain anesthesia clinically. Systematically increasing the GA concentration for our approximately 70 000 plausible parameter sets resulted in the expected fractional increases in θ and δ activity, as well as fractional decrease in α. But the majority of parameter sets did not exhibit the transient surge in total EEG power characteristic of the so-called "biphasic" response. Eighty-six "biphasic" parameter sets were then selected by requiring a substantial increase in total power (1.4 times baseline) at 1 MAC equivalent isoflurane concentration. For these parameter sets the 90% and 95% spectral edge frequencies clearly showed monotonic reductions with increasing anesthetic concentration.

In contrast, such an effect was absent in the majority of unselected sets. This result together with the clear difference in sensitivity profiles of "biphasic" and "nonbiphasic" sets suggests that additional constraints exist that have not yet been explicitly incorporated in our theory. From an experimental perspective the discriminating ability of the sensitiv-

TABLE V. A selection of 12 parameter sets for Eqs. (1)–(6) and (12) out of those 86 showing a strong "biphasic" power rise; see Sec. V B. Parameters not listed here should be chosen according to Table I. $h_e^*=(1+x_e)h_e^r$ is the chosen solution of Eqs. (18) and (19). The data in Table 3 of Ref. [54] have inspired this particular selection; see Fig. 12. But those data have not been used for determining the original 86 parameter sets.

h_e^r (mV)	−70.152	−75.083	−71.915	−78.549	−62.822	−67.265	−63.677	−64.451	−62.038	−74.179	−72.293	−79.078
h_i^r (mV)	−65.557	−66.323	−76.042	−76.432	−71.634	−76.182	−74.307	−78.210	−64.990	−62.177	−67.261	−74.426
τ_e (ms)	126.05	129.78	105.51	126.46	48.686	81.979	53.688	122.52	133.08	81.961	32.209	129.02
τ_i (ms)	131.15	116.53	149.00	145.13	143.21	65.665	117.42	126.89	96.501	143.39	92.260	77.340
h_{ee}^{eq} (mV)	−16.422	−12.416	−9.0033	−10.722	−5.7406	−18.154	1.5068	−10.018	−5.4389	−16.256	7.2583	−16.855
h_{ei}^{eq} (mV)	−18.587	8.1660	−10.326	6.3858	−14.169	−4.9348	−1.2171	−10.040	−7.6872	−8.6829	9.8357	−0.60817
h_{ie}^{eq} (mV)	−83.601	−82.724	−87.476	−84.666	−77.014	−85.493	−87.907	−83.947	−79.655	−78.006	−80.697	−86.897
h_{ii}^{eq} (mV)	−77.778	−85.746	−82.275	−83.481	−87.580	−88.833	−85.931	−87.552	−85.636	−79.480	−76.674	−80.248
Γ_{ee} (mV)	1.1204	0.23631	0.29348	1.7299	0.32694	0.11884	0.10831	0.36844	0.46193	0.32740	0.29835	0.32204
Γ_{ei} (mV)	1.7901	1.9680	1.8455	1.5275	1.3505	0.27110	1.3641	1.2134	0.90863	0.47183	1.1465	0.98323
Γ_{ie} (mV)	1.6079	1.2128	1.9915	1.7976	1.3704	1.8885	1.4293	1.5182	0.86035	0.77945	1.2615	1.7386
Γ_{ii} (mV)	0.38521	0.36550	0.35259	0.81632	0.98025	0.28057	0.10257	0.24242	0.19125	0.98994	0.20143	0.64509
γ_{ee} (s^{-1})	536.71	594.06	841.18	989.31	826.47	359.89	656.33	133.46	939.65	125.36	122.68	595.98
γ_{ei} (s^{-1})	950.75	487.60	859.70	728.78	906.57	897.73	800.05	257.09	717.38	627.14	982.51	930.15
γ_{ie} (s^{-1})	470.98	309.93	451.66	249.88	446.06	310.45	389.73	485.09	469.46	210.53	293.10	69.449
γ_{ii} (s^{-1})	112.12	89.657	84.790	112.91	85.636	96.192	87.991	111.17	106.88	129.72	111.40	61.290
N_{ee}^{β}	2495.0	3995.4	2194.0	2509.5	2008.4	3639.7	2603.2	2678.1	4570.7	2786.6	4202.4	2277.8
N_{ei}^{β}	4425.7	3678.7	4752.2	3401.1	4750.0	3869.3	3811.6	4575.8	4176.1	2802.0	3602.9	2503.1
N_{ie}^{β}	523.75	106.34	699.60	742.06	582.01	514.24	224.58	373.09	505.21	551.59	443.71	203.01
N_{ii}^{β}	519.43	233.08	515.95	770.87	385.87	548.39	591.88	626.57	523.02	288.92	386.43	504.47
N_{ee}^{α}	4169.6	4084.8	3668.7	4208.0	2031.0	3591.9	3505.2	3060.9	2966.6	2149.5	3228.0	4967.6
N_{ei}^{α}	2099.0	1032.9	1033.0	1452.3	1099.4	2005.9	1247.4	2081.2	1141.5	2448.7	2956.9	1347.6
Λ (cm^{-1})	0.74744	0.11922	0.34501	0.33835	0.31505	0.28265	0.84744	0.80260	0.21252	0.96933	0.60890	0.94826
v (cm^{-1})	648.82	246.22	780.67	754.34	218.00	673.72	234.51	901.10	481.67	743.94	116.12	984.15
$S_e^{\max}$ (s^{-1})	73.134	363.20	355.24	149.33	67.222	87.005	81.612	58.463	83.887	222.71	66.433	272.80
$S_i^{\max}$ (s^{-1})	182.39	121.55	424.78	51.599	233.78	176.30	52.578	312.88	363.52	122.30	393.29	142.84
$\overline{\mu_e}$ (mV)	−43.383	−53.610	−52.279	−40.604	−42.869	−48.925	−53.577	−41.437	−43.611	−51.129	−44.522	−47.867
$\overline{\mu_i}$ (mV)	−46.960	−45.360	−48.592	−53.120	−42.052	−49.717	−42.697	−49.024	−40.450	−51.109	−43.086	−47.732
$\hat{\sigma}_e$ (mV)	4.2840	4.2660	4.9083	6.1417	6.7898	6.7627	4.6999	2.2834	4.3683	4.4783	4.7068	6.7860
$\hat{\sigma}_i$ (mV)	2.9594	5.1212	3.6979	2.7247	4.0164	6.9368	4.6956	3.9589	4.8866	4.8342	2.9644	3.9343
$\overline{p_{ee}}$ (s^{-1})	2258.1	8992.9	6024.9	4662.4	2288.9	8924.6	5975.4	2117.7	8041.4	4804.5	2250.6	204.95
p_{ei} (s^{-1})	1139.6	385.28	1115.6	2693.2	212.00	2025.0	8684.6	98.487	530.95	2642.8	4363.4	3041.8
h_e^* (mV)	−56.859	−71.569	−71.877	−62.223	−58.604	−61.278	−66.274	−48.905	−54.966	−65.452	−59.661	−68.424

ity analysis may suggest ways in which the mechanism of GA can be studied at conveniently low anesthetic concentrations.

We briefly return to the related theory of Steyn-Ross *et al.* [6], because a comparison allows us to elucidate a number of crucial advantages of the model presented here. Steyn-Ross *et al.* adiabatically reduced Eqs. (1)–(6) in homogeneous form to a system of two coupled nonlinear ordinary differential equations, and then studied their linearized white noise fluctuation spectrum. Qualitatively, a "biphasic" effect was produced showing hysteresis between the "induction" and "recovery" phases of anesthesia. The basis for both the surge in low-frequency power ("critical slowing") and the hysteresis is attributable to their system moving between different stable null-cline branches. This implies that firing rates, and by definition the mean soma membrane potentials, are expected to vary nonsmoothly with anesthetic level, a prediction not borne out experimentally. Comprehensive studies [51] indicate that GAs reduce spontaneous action potential firing in a relatively smooth dose-dependent manner.

In contrast, our theory does not require leaving a stable branch in order to obtain a surge in total EEG power. Indeed, the majority of physiological plausible dynamics occurs with parametrizations exhibiting only *one* stable low firing rate singular point. Even in the minority of cases where multiple singular points are found, population neural firing activity should always be in accord with experimental rates typically between 0.1 to 20 pulses per second (pps) (see for example Refs. [52,53]). In contrast Steyn-Ross *et al.* have *resting* excitatory and inhibitory neuronal firing rates, at zero anes-

TABLE VI. A selection of 12 parameter sets for Eqs. (1)–(6) and (12) out of those 73 368 *not* showing a strong "biphasic" power rise; see Sec. V B. Parameters not listed here should be chosen according to Table. I. $h_e^*=(1+x_e)h_e^r$ is the chosen solution of Eqs. (18) and (19). The data in Table 3 of Ref. [54] have inspired this particular selection; see Fig. 12. But those data have not been used for determining the original 73 368 parameter sets.

h_e^r (mV)	−79.301	−74.262	−73.375	−74.809	−63.009	−67.309	−68.008	−77.897	−73.148	−78.504	−74.887	−69.468
h_i^r (mV)	−65.658	−70.219	−72.156	−74.010	−77.819	−69.499	−64.406	−61.485	−63.755	−74.825	−70.819	−65.402
τ_e (ms)	74.633	11.787	65.733	42.183	43.667	120.29	51.353	114.34	148.18	112.02	64.389	15.060
τ_i (ms)	116.48	138.25	77.238	77.991	48.614	85.927	139.91	120.98	110.45	130.87	102.88	45.711
h_{ee}^{eq} (mV)	−1.7913	−12.998	−6.1453	−9.4775	−8.3898	1.4387	0.10317	−15.478	−12.312	0.19506	−5.0918	1.5372
h_{ei}^{eq} (mV)	−8.9948	−18.516	−6.8789	2.3501	−12.819	−7.6350	0.89281	−17.960	−9.7025	9.6042	−7.5187	−12.830
h_{ie}^{eq} (mV)	−84.503	−81.389	−85.087	−82.383	−86.471	−78.148	−76.314	−84.965	−70.637	−86.581	−86.376	−76.218
h_{ii}^{eq} (mV)	−86.279	−82.898	−84.564	−83.772	−86.492	−89.533	−80.368	−87.456	−86.168	−81.842	−80.451	−78.381
Γ_{ee} (mV)	0.79070	0.92695	0.25283	0.55879	0.11685	1.2015	0.29420	0.62454	0.24586	0.55290	0.67576	0.54214
Γ_{ei} (mV)	1.8752	1.3012	1.7238	1.8244	1.3761	1.3415	0.68088	1.9905	1.5104	0.75036	1.6601	1.2301
Γ_{ie} (mV)	1.7374	0.19053	1.6983	1.0051	0.61087	1.9721	1.6722	1.5395	0.39485	1.4952	1.8018	1.3222
Γ_{ii} (mV)	0.93418	0.94921	0.21967	0.70799	1.1084	1.9578	0.86047	1.0311	1.8980	0.68146	1.2419	1.7150
γ_{ee} (s^{-1})	911.23	816.04	238.83	854.84	585.52	971.10	351.64	947.55	703.62	196.69	405.30	601.75
γ_{ei} (s^{-1})	263.64	261.29	188.92	421.82	254.60	571.17	406.30	491.92	426.65	106.67	314.96	194.64
γ_{ie} (s^{-1})	415.20	219.09	485.66	314.93	294.38	125.79	335.58	447.17	202.25	265.16	390.34	203.81
γ_{ii} (s^{-1})	37.922	40.575	32.659	44.507	28.351	49.013	54.252	50.021	38.169	49.030	54.273	28.176
N_{ee}^{β}	2493.0	3893.0	2682.7	2654.2	3169.8	3246.2	2335.5	2957.5	2013.8	2290.9	4234.6	4492.9
N_{ei}^{β}	2133.1	3326.8	2433.8	3030.1	4349.8	2539.9	2823.5	4689.2	3601.3	2285.6	4440.1	4172.5
N_{ie}^{β}	952.04	839.39	959.11	466.65	883.26	822.84	933.82	758.36	804.38	257.81	839.75	482.48
N_{ii}^{β}	691.83	682.41	337.13	211.81	129.65	745.97	692.24	289.56	146.48	222.87	578.24	952.66
N_{ee}^{α}	3410.9	4013.5	3813.4	2729.3	2716.7	2629.3	3177.9	2367.2	4471.2	2055.0	2296.0	3571.4
N_{ei}^{α}	2775.8	1544.3	2183.2	2482.7	1965.8	1784.8	1211.5	1619.0	1603.3	2165.3	1811.2	2769.0
Λ (cm^{-1})	0.85707	0.96545	0.36352	0.61940	0.37098	0.64873	0.66420	0.98304	0.12448	0.38379	0.80136	0.34765
v (cm^{-1})	106.68	101.78	332.11	776.27	161.41	636.07	475.32	125.41	953.10	513.42	795.75	317.83
$S_e^{\max}$ (s^{-1})	196.17	266.44	291.86	231.51	398.31	335.82	307.69	462.24	253.15	402.81	267.50	102.61
$S_i^{\max}$ (s^{-1})	389.24	300.65	377.27	183.69	252.23	257.93	397.24	183.35	145.59	53.402	344.75	475.63
$\overline{\mu_e}$ (mV)	−53.020	−43.634	−44.648	−42.756	−40.859	−45.007	−41.154	−41.903	−46.486	−42.852	−48.084	−43.695
$\overline{\mu_i}$ (mV)	−42.091	−50.836	−40.912	−52.535	−46.798	−49.958	−52.219	−51.854	−54.379	−49.230	−54.688	−42.247
$\hat{\sigma}_e$ (mV)	6.2966	5.6536	6.6687	6.4016	3.7178	3.0158	5.3708	6.7661	6.2127	5.6446	4.7320	4.8791
$\hat{\sigma}_i$ (mV)	4.6483	3.3140	3.3770	3.2945	2.4196	3.2253	3.2753	3.0434	3.7758	4.4832	3.6845	2.7574
$\overline{p_{ee}}$ (s^{-1})	4406.3	83.190	2133.2	4087.4	9225.2	9379.7	9909.2	9265.9	5073.9	4381.4	2073.4	983.37
p_{ei} (s^{-1})	4133.7	6407.5	4219.3	3031.3	5932.3	8900.6	7011.4	3023.7	165.84	7775.2	1387.0	2303.9
h_e^* (mV)	−79.764	−72.299	−79.743	−73.618	−62.403	−61.811	−65.271	−78.263	−69.261	−70.227	−72.334	−66.541

thetic concentration, always greater than $S_e^{\max}/2$ and $S_i^{\max}/2$, respectively. For their parametrizations this is typically greater than 250 pps. Furthermore, they parametrize anesthetic action only by scaling inhibitory neuronal rate constants (i.e., $\gamma_{lk}\rightarrow\gamma_{lk}/\lambda$) in an adiabatically reduced model incapable of exhibiting any physiological α resonance. Our model delivers the complete spectral content observed in human EEG, appropriate mean firing rates, yet "biphasic" rises in total EEG power can occur within meaningful physiological and pharmacological domains.

A number of further advances can be made based on the work performed in this paper. More stringent experimental constraints, in particular with regard to the GA modeling, can remove much of the remaining uncertainty in the predictions. Many insights will be gained from the comparison of the predicted effects for different GA agents, once appropriate data is available. Even now it appears feasible to fit our model predictions quantitatively to experimental EEG data. As an outlook, we present in Fig. 12 a rough comparison. See the appendix for the details. However, we believe that dedicated experiments in which the theoretical modelers are closely involved are necessary. Otherwise it appears nearly impossible to disentangle failures of the model from vagaries of the experimental procedure, in particular if the data are taken in an operating theater full of noisy electronic equipment. In this respect the possibility of performing studies with low concentrations of GAs, as suggested by our sensitivity study, may become very useful.

Furthermore, there still remain some fundamental concerns about *what* one should attempt to model. For example, we have not addressed at all the issue of possible hysteresis in EEG total power surges with regard to the induction and recovery phase. At this point in time it is unclear whether such hysteresis is not just a reflection of pharmacokinetics. We may be able to shed light on this issue with our full grid simulations, which showed sensitivity to the speed of GA concentration change. In the long run we may be able to determine the parameter set corresponding to the brain of a patient with sufficient precision to predict his or her individual response to a range of GAs with an accuracy useful to researchers of consciousness and medical practitioners.

ACKNOWLEDGMENTS

We thank Professor P. J. Cadusch for helpful discussions and M. P. Dafilis for providing Fig. 3. I.B. is supported by Grant No. DP0209218 from the Australian Research Council. We are grateful for the use of the facilities of the Swinburne Centre for Supercomputing and Astrophysics and the Victorian Partnership for Advanced Computing.

APPENDIX: PARAMETER TABLES

The complete collection of 73 454 plausible parameter sets is available on request, as is the subset of 86 parameter sets showing a strong "biphasic" power rise. However, it seems appropriate to list here some exemplars of these sets for immediate use. A selection of 12 parameter sets out of the 86 "biphasic" ones can be found in Table V. To represent the majority of other parameter sets, Table VI collects 12 "nonbiphasic" ones. In order to arrive at the selections in a nonarbitrary manner, we have compared results derived from the eigenspectra of these sets with the isoflurane data in Table 3 of Ref. [54]. Thus we have computed and compared the mean and standard deviation of SEF_{90}, total power, and δ, θ, α, and β band fractional power for these selections.

Given the impossibility of investigating $\binom{86}{12}$ or even worse $\binom{73\,368}{12}$ unique combinations, we have just endeavored to find selections matching these data "better than average." Furthermore, the original parameter searches were not tailored to this data. Hence these selections do not represent a best fit of our theory to this data. Proper comparisons with experimental data will be the topic of a future paper. With those caveats in mind, it is nevertheless instructive to see how well these selections compare with the data. The bands in Fig. 12 represent this time not quantiles, but means (middle line) and standard deviations (edges). This allows direct comparison with the means and standard deviations of data taken from 12 patients [54]. The dark bands in Fig. 12 represent the selection of Table V, the light ones are calculated from the selection in Table VI.

The comparison is nontrivial for total power: The appropriate constant of proportionality for relating our h_e and the experimental EEG amplitude of Ref. [54] is unknown in practice. Furthermore, for linear eigenspectrum predictions $h_e \propto \delta p_{ee}$ and thus its *absolute* value is as uncertain as the constant of extracortical noise variance δp_{ee}. An upper limit for δp_{ee} could be obtained by requiring consistent linearity in full grid simulations, but we have not attempted this here. Instead total power has been normalized to its value at zero concentration. Hence agreement there is by construction and comparisons should be made only at higher concentrations.

The "biphasic" selection provides a decent description of SEF_{90}, total power, and δ fractional power. The large standard deviation of the δ predictions at higher concentrations devalues the agreement there somewhat. Also predicted total power follows the experimental trend well, but appears systematically lower than experiment. Among the unselected "biphasic" parameter sets some have stronger power surges, but did not improve the overall agreement. In contrast, the "nonbiphasic" selection fails completely with regards to SEF_{90} and total power. Concerning the fraction of power in the δ band, the "nonbiphasic" selection agrees but seems to have the wrong concentration trend. The reverse situation occurs for θ, α, and β fractional power. Here the "biphasic" selection clearly fares worse than the "nonbiphasic" one.

However, the concentration trend in β is actually better described by the "biphasic" selection. A constant increase of the β fraction of power by about 8% would mean very good agreement. A corresponding decrease in α at low concentrations and in θ at high concentrations would result in a good overall fit for the "biphasic" set. A dedicated search for matching parameter sets might ameliorate these problems.

One can also speculate that there is some contamination in the shown experimental data. If some of the observed power in the β band stems from noncortical sources, e.g., is an artifact of muscle movements, then the deviations may be artificial. In particular the data showing a constant power fraction in the α band are curious. One could reasonably expect some decrease at higher concentrations. On the other hand, there is a clear power rise in the data and thus the "nonbiphasic" selection is clearly disfavored.

[1] O. R. Ryynanen, J. A. Hyttinen, P. H. Laarne, and J. A. Malmivuo, IEEE Trans. Biomed. Eng. **51**, 1547 (2004).

[2] M. van Gils, I. Korhonen, and A. Yli-Hankala, Crit. Rev. Biomed. Eng. **30**, 99 (2002).

[3] P. S. Myles, K. Leslie, J. McNeil, A. Forbes, and M. T. Chan, Lancet **363**, 1757 (2004).

[4] P. S. Sebel, E. Lang, I. J. Rampil, P. F. White, R. Cork, M. Jopling, N. T. Smith, P. S. Glass, and P. Manberg, Anesth. Analg. **84**, 891 (1997).

[5] J. M. Evans, in *Consciousness, Awareness and Pain in General Anaesthesia*, edited by M. Rosen and J. N. Lunn (Butterworth, London, 1987), pp. 18–34.

[6] M. L. Steyn-Ross, D. A. Steyn-Ross, J. W. Sleigh, and D. T. J. Liley, Phys. Rev. E **60**, 7299 (1999).

[7] C. H. Ting, A. Angel, and D. A. Linkens, Biol. Cybern. **88**, 99 (2003).
[8] D. T. J. Liley, P. J. Cadusch, and M. P. Dafilis, Network Comput. Neural Syst. **13**, 67 (2002).
[9] D. T. J. Liley, P. J. Cadusch, and J. J. Wright, Neurocomputing **26–27**, 795 (1999).
[10] I. Bojak, D. T. J. Liley, P. J. Cadusch, and K. Cheng, Neurocomputing **58–60**, 1197 (2004).
[11] P. L. Nunez, *Neocortical Dynamics and Human EEG Rhythms* (Oxford University Press, New York, 1995).
[12] P. L. Nunez, *Electric Fields of the Brain: The Neurophysics of EEG*, 1st ed. (Oxford University Press, New York, 1981).
[13] P. A. Robinson, P. N. Loxley, S. C. O'Connor, and C. J. Rennie, Phys. Rev. E **63**, 041909 (2002).
[14] V. K. Jirsa and H. Haken, Phys. Rev. Lett. **77**, 960 (1996).
[15] P. L. Nunez, Brain Topogr **1**, 199 (1989).
[16] R. D. Traub, J. G. R. Jefferys, and M. A. Whittington, *Fast Oscillations in Cortical Circuits* (MIT Press, Cambridge, MA, 1999).
[17] A. Gottschalk and P. Haney, Anesthesiology **98**, 548 (2003).
[18] U. Rudolph and B. Antkowiak, Nat. Rev. Neurosci. **5**, 709 (2004).
[19] J. P. Dilger, Br. J. Anaesth. **89**, 41 (2002).
[20] C. Vahle-Hinz and O. Detsch, Br. J. Anaesth. **89**, 123 (2002).
[21] M. D. Krasowski and N. L. Harrison, Cell. Mol. Life Sci. **55**, 1278 (1999).
[22] N. P. Franks and W. R. Lieb, Toxicol. Lett. **100–101**, 1 (1998).
[23] S. L. M. de Sousa, R. Dickinson, W. R. Lieb, and N. P. Franks, Anesthesiology **92**, 1055 (2000).
[24] C. D. Richards, Br. J. Anaesth. **89**, 79 (2002).
[25] X.-S. Wu, J.-Y. Sun, A. S. Evers, M. Crowder, and L.-G. Wu, Anesthesiology **100**, 663 (2004).
[26] B. Antkowiak, Br. J. Anaesth. **89**, 102 (2002).
[27] K. Kuizenga, C. J. Kalkman, and P. J. Hennis, Br. J. Anaesth. **80**, 725 (1998).
[28] E. R. John, L. S. Prichep, W. Kox, P. Valdes-Sosa, J. Bosch-Bayard, E. Aubert, M. Tom, F. di Michele, and L. D. Gugino, Conscious Cogn **10**, 165 (2001); **11**, 138(E) (2002).
[29] M. I. Banks and R. A. Pearce, Anesthesiology **90**, 120 (1999).
[30] M. B. MacIver, A. A. Mikulec, S. M. Amagasu, and F. A. Monroe, Anesthesiology **85**, 823 (1996).
[31] K. Nishikawa and M. B. MacIver, Anesthesiology **92**, 228 (2000).
[32] M. I. Banks (private communication).
[33] E. R. Kandel, J. H. Schwartz, and T. M. Jessel, *Principles of Neural Science*, 4th ed. (McGraw-Hill, New York, 2000).
[34] N. P. Franks and W. R. Lieb, Anesthesiology **84**, 716 (1996).
[35] W. W. Mapleson, Br. J. Anaesth. **76**, 179 (1996).
[36] M. P. Dafilis, D. T. J. Liley, and P. J. Cadusch, Chaos **11**, 474 (2001).
[37] M. P. Dafilis, P. D. Bourke, D. T. J. Liley, and P. J. Cadusch, Comput. Graph. **26**, 971 (2002).
[38] Computer Code MINUIT (CERN Computing and Networks Division, CERN, Geneva, 1994), version 94.1.
[39] R. Eberhart and J. Kennedy, in Proceedings of the Sixth International Symposium on Micro Machine and Human Science, Nagoya, Japan, 1995 (IEEE, Piscataway, NJ), pp. 39–43.
[40] A. Carlisle and G. Dozier, in Proceedings of the 2001 Workshop on Particle Swarm Optimization, Indianapolis, 2001 (IEEE, Piscataway, NJ), pp. 1–6.
[41] I. Bojak (unpublished).
[42] Computer code MPI-1.2 FORTRAN (Message-Passing Interface Forum, 1997), http://www.mpi-forum.org.
[43] T. Iijima, Z. Nakamura, Y. Iwao, and H. Sankawa, Anesth. Analg. **91**, 989 (2000).
[44] G. McPherson, *Applying and Interpreting Statistics: A Comprehensive Guide*, 2nd ed. (Springer, New York, 2001).
[45] W. J. Freeman, Biol. Cybern. **56**, 139 (1987).
[46] A. Rotterdam, F. H. Lopes da Silva, J. van der Ende, M. A. Viergever, and A. J. Hermans, Bull. Math. Biol. **44**, 283 (1982).
[47] C. J. Stam, J. P. Pijn, P. Suffczynski, and F. H. Lopes da Silva, Clin. Neurophysiol. **110**, 1801 (1999).
[48] I. J. Rampil, Anesthesiology **89**, 980 (1998).
[49] H. Schwilden and C. Jeleazcov, J. Clin. Monit Comput. **17**, 449 (2003).
[50] A. Miller, J. W. Sleigh, J. Barnard, and D. A. Steyn-Ross, Br. J. Anaesth. **92**, 8 (2004).
[51] B. Antkowiak, Anesthesiology **91**, 500 (1999).
[52] H. Hirase, X. Leinekugel, A. Czurko, J. Csicsvari, and G. Buzsaki, Proc. Natl. Acad. Sci. U.S.A. **98**, 9386 (2001).
[53] L. Marshall, D. A. Henze, H. Hirase, X. Leinekugel, G. Dragoi, and G. Buzsaki, J. Neurosci. **22**, RC197 (2002).
[54] D. Schwender, M. Daunderer, S. Klasing, U. Finsterer, and K. Peter, Anaesthesia **53**, 335 (1998).